An application of the boundary element method (BEM) to the calculation of the single-scattering properties of very complex ice crystals in the microwave and sub-millimetre regions of the electromagnetic spectrum

Article

It is advisable to refer to the publisher's version if you intend to cite from the work. See Guidance on citing.

www.reading.ac.uk/centaur

CentAUR

Central Archive at the University of Reading

Reading's research outputs online

An application of the boundary element method (BEM) to the calculation of the single-scattering properties of very complex ice crystals in the microwave and sub-millimetre regions of the electromagnetic spectrum

Antigoni Kleanthous[a], Anthony J. Baran[b,c], Timo Betcke[a], David P. Hewett[a], Christopher D. Westbrook[d]

[a]*University College London, Department of Mathematics, London, UK*
[b]*Met Office, Exeter, UK*
[c]*University of Hertfordshire, School of Physics, Astronomy, and Mathematics, Hertfordshire, UK*
[d]*University of Reading, Department of Meteorology, UK*

Abstract

To improve the prediction of weather and climate models there is a need for the accurate computation of the single-scattering properties of randomly oriented complex atmospheric ice crystals. Here, we apply BEM to calculate these properties in the microwave and sub-millimetre region of the electromagnetic spectrum for the purposes of all-sky data assimilation. The properties are calculated at the frequencies of 50, 183, 243 and 664 GHz for the temperatures of -83°C, -43°C, and -3°C. The particles are assumed to be complex aggregates of bullet rosettes with maximum dimensions that vary between 10 and 10,000μm. Moreover, the rosette-aggregates are constructed to follow an observed mass-dimension power law that is consistent with an ice microphysics scheme in a weather model. To solve efficiently the BEM linear matrix equation, random orientation is simulated by fixing the particle with respect to the incident plane wave with the latter rotated about the particle. This representation is shown to replicate T-matrix solutions found for hexagonal columns to within a few percent for size parameters between 0.05 and 10. We further show that we can simulate the single-scattering properties with errors less than a few percent, using only 14 and up to 302 incident waves for the smallest and largest size parameters respectively. The errors grow larger only for some of the largest size parameters considered. We find that BEM can be applied to compute accurately the scattering properties of complex ice aggregates of importance to weather and climate models.

Keywords: Electromagnetic scattering; Absorption; Microwave; Remote sensing; Weather; Climate; Boundary Element Method

1. Introduction

To improve Numerical Weather Prediction (NWP) models it is generally considered necessary to assimilate all-sky microwave radiances into those models to ameliorate their predictive quality of weather events [1, 2]. There is particular interest in all-sky microwave data assimilation at the moment owing to the launch in about 2025 of the Ice Cloud Imager (ICI), as part of the next generation of European polar orbiting weather satellites, which will provide daily observations of cloud ice [3]. The novelty of the ICI instrument is that it will consist of cloud ice sensing frequencies between 183 and 664 GHz, and will be the first operational weather instrument to have cloud sensing frequencies beyond 200 GHz, inclusive of full polarisation measurements at 243 and 664 GHz. However, the process of using cloudy radiance observations provided by space-based instruments such as ICI requires knowledge about the macrophysics and microphysics properties of ice clouds, as well as the scattering and absorption properties of the cloud ice hydrometeors [4, 5, 6, 1, 7, 8]. This knowledge requirement is problematic as it is well-known that cloud ice hydrometeors consist of non-spherical particles that can vary significantly in terms of their shapes and sizes [9, 10, 11, 12]. Therefore, to take advantage of the observations provided by ICI it is necessary to develop electromagnetic methods that can be applied to the variety of hydrometeor shapes and sizes that occur in cirrus and ice cloud so their single-scattering properties can be efficiently solved for.

To this end, a number of different approaches are used by the atmospheric physics community for the simulation of electromagnetic dielectric scattering, depending on the size parameter of the problem. For particles of small to moderate size parameter there are "numerically exact" methods [13] such as the Discrete Dipole Approximation (DDA) [14, 15], the Finite-Difference Time-Domain (FDTD) [16, 17, 18] and Pseudo-Spectral Time-Domain (PSTD) [19] methods, and the Extended Boundary Condition [20, 21, 22] and Invariant Imbedded [23, 24] T-matrix methods. For particles of large size parameter one can use "approximate" high-frequency methods such as Geometric Optics/ray tracing and the Kirchhoff approximation (see e.g. [25, 26, 27, 28, 29, 30, 31, 32, 33, 34, 35, 36]).

Given the range of the sensing frequencies of the ICI, a numerical method that can handle both low and high frequencies (or small and large size parameter problems respectively) is of interest and the boundary element method (BEM) is appealing in this case as it poses no restrictions on the shape of the scatterer, apart from Lipschitz continuity. BEM is a "numerically exact" method that allows us to solve certain types of partial differential equations (PDEs) in homogeneous bounded/unbounded media. It involves reformulating the PDE in terms of integral equations on the boundary of the object of interest, the scatterer. The boundary of the scatterer is subsequently discretised and the boundary integral equation (BIE) is transformed into a system of linear equations which can be solved using some direct or iterative method. Depending on the problem of interest, the solution can then be extended from the boundary to the interior, exterior or far field of the scatterer via representation formulae.

There are a number of advantages to using BEM compared to other numerical methods. By reformulating the PDE as a system of boundary integral equations one reduces the dimensionality of the problem from a 3D scatterer to a 2D manifold (generally speaking of an arbitrary domain - the scatterers studied here are piecewise differentiable). The discretisation of the 2D manifold is faster and easier to achieve compared to that of a 3D domain and leads to a smaller system of equations that needs to be solved. At the same time, BEM automatically incorporates the radiation condition at infinity. On the other hand, the discretisation of BEM leads to matrices that are usually dense, requiring fast approximation methods such as $\mathcal{H}$-matrices [37], $\mathcal{H}^2$-matrices [38, 39, 40] or Fast Multipole Methods (FMM) [41, 42, 43]. However, BEM can handle complicated geometries making it appealing for scattering problems by complex domains, such as those that occur in cirrus and ice cloud.

The PMCHWT formulation (due to Poggio, Miller, Chang, Harrington, Wu and Tsai [44, 45, 46, 47]), is one of the most commonly used BIE formulations for the simulation of electromagnetic scattering by dielectric objects [48, 49, 50, 51, 52, 53, 54, 55] and is the formulation used here. However, it leads to ill-conditioned linear systems under Galerkin discretisation, and Calderón preconditioning [48, 49, 50, 51, 54, 55], an operator-based approach [56], can be used to remedy this. To obtain a stable discretisation of the operator products that arise in this approach, the use of a dual mesh defined on a barycentrically refined grid needs to be considered [57], increasing memory consumption. Furthermore, to capture the oscillatory solution of the electromagnetic waves, the mesh needs to be refined with respect to frequency [52], making the simulation of high-frequency problems very expensive until recently. New developments accelerating Calderón preconditioning [54, 55], that reduced computational time and memory, have alleviated the otherwise prohibitive cost allowing us to consider high frequency scattering by realistic complex shaped domains.

The boundary element method has already started getting attention in the atmospheric physics community, but without the use of preconditioning and accelerating techniques, applications of BEM were restricted to simple domains (e.g. [58, 59, 60]) or small size parameters (e.g. [52, 53]). With the use of the accelerating techniques [54, 55] that minimise memory consumption, assembly time and solve time, applications of BEM on oriented complex-shaped ice-crystals of higher size parameters (up to 70) were considered in [54, 55]. Complex aggregates consisting of several monomers with little or zero separation touching at single points (for example bullet rosettes and aggregates of those) were treated as a multi-particle scattering problem taking advantage of reduced versions of Calderón preconditioners that were better suited for multi-particle configurations instead of treating the aggregate as a single scatterer [54]. The accelerating methods of [55] have demonstrated a 99% reduction in memory cost and at least 80% in computation time, for the highest frequency considered (664 GHz). Using the accelerating techniques of [54, 55] we are now able to apply BEM to compute the single-scattering properties (SSPs) of randomly-oriented budding rosettes and rosette aggregates, at a range of maximum dimensions and frequencies.

A number of microwave-based SSPs of randomly oriented ice crystals available for utilisation in NWP models and in remote-sensing exist. For instance, the SSPs provided by Liu [61] and Hong *et al.* [62] used the DDA method, which at the time limited either the range in frequency or temperature that those studies could consider. In the case of [61], frequencies beyond 340 GHz were not considered, and in the case of [62] a single temperature of -30°C was assumed. In contrast to this, [61] considered four temperatures between -40 and 0°C. However, both studies consider a broad range of ice particle shapes ranging from solid hexagonal columns and plates, hollow hexagonal columns, three-dimensional bullet rosettes, sector snowflake models, and aggregates of hexagonal columns, among others.

More recent microwave SSPs of randomly oriented non-spherical ice crystals have been provided by Ding *et al.* [63] who applied the invariant imbedding T-matrix and Improved Geometric Optics methods at the smaller and larger size parameters to calculate the SSPs, respectively. These methods were applied to solid and hollow hexagonal columns, solid plates, solid and hollow bullet rosettes, and aggregates of plates and columns, among others, to solve for their SSPs. The frequencies and maximum dimensions of ice crystals considered in this study range from 1 to 874 GHz, and between 2 and $10000\mu m$, respectively, where the maximum dimensions of the ice crystals are distributed in twenty four size bins. The SSPs were calculated assuming four temperature values between -113 and -3°C.

Another set of non-spherical ice SSPs for application in NWP and remote-sensing has been put forward by Eriksson *et al.* [64], which includes the full Stokes vector between the frequencies of 1 and 886 GHz for three temper-

ature values of -83°C, -43°C, and -3°C. In [64], it was concluded that three temperature values were sufficient for interpolation between the coldest and warmest temperature values to obtain SSPs at all other possible temperatures. This set of SSPs consist of thirty four types of particle assuming random orientation using the DDA alone to compute the SSPs of all the particle models between the sizes of 10 and up to $20000\mu m$ for some of the ice crystal models but not all, comprising of about 30 sizes per ice crystal shape. The ice crystal shapes considered are both single and aggregated ice crystals. The single ice crystal shapes consist of seven types of hexagonal columns and plates and six varieties of bullet rosettes, among others. The aggregated ice crystals consist of nine different variations of ice crystal aggregations, including the dendrite model of [65]. The database of [64] has already been implemented by Moradi *et al.* [66] into an all-sky radiative transfer forward operator for data assimilation in numerical weather prediction, building on earlier work by Stegmann *et al.* [67] and Tang *et al.* [68].

The distinguishing feature of this set ([64]) of SSPs to that proposed by [62] is that the ice crystal aggregates follow differing mass-dimension power laws and possess fractal-like behaviour so that the mass of the ice crystal is proportional to its maximum dimension raised to the power of approximately two. It is now well-known that the mass of ice crystal aggregations ought to follow such a power law as found in the studies by [69, 70, 71, 72, 73, 12]. However, in the observational aircraft-based closure study by Fox *et al.* [8] it was shown that no one ice crystal model proposed by [64] could replicate the simultaneous microwave and sub-millimetre observations between 183 and 664 GHz obtained from over a few cases of mid-latitude cirrus. This closure study demonstrates that even if the masses of the ice crystal models were constrained by in-situ measurements of the bulk ice mass, the particle size distributions, and habits as a function of distance from the cloud top it is still very difficult to replicate the measurements from across the microwave and sub-millimetre spectrum using current microwave SSPs.

In an attempt to circumvent the need for SSPs of many differing ice crystal types, which for each size of such a variety of habits is onerous to compute, the work of [7] proposed an alternative approach. In that study, it was shown that a three-component model of ice cloud bounded the SSPs of the aggregate ice crystals and hollow bullet rosettes from the Ding *et al.* [63] database between the frequencies of 89 and 874 GHz. As the three-component model bounded the SSPs of a diverse range of ice crystal masses, it was argued that this simpler approach could be sufficient to replicate microwave observations such as those provided by Fox *et al.* [8]. More recently, Sun *et al.* [74] have proposed to represent the ensemble of shapes by superspheroids to act as surrogates for the real ice crystals that occur in the Earth's atmosphere. This is done by specifying a shape index for the superspheroid, which is defined as the ratio of the volume-to-projected area of

the real ice crystal. The study shows that at thirty three microwave bands between 3 and 640 GHz, and at three important bands in the visible and infrared, the superspheroid approximation can mimic the SSPs of realistic ice crystals to within reasonable accuracy as long as the ice aggregates are compact rather than sparse. It is yet to be seen if approximations such as those proposed by the two previous studies can simulate microwave and sub-millimetre observations to within reasonable accuracy relative to alternative more complex models.

As found by [8], using present microwave SSPs it has not been possible to replicate all the current microwave and sub-millimetre observations from across the microwave spectrum used in that study, even if the macrophysics and microphysics of several clouds are well characterised. This is why alternative microwave SSPs to those that are currently available are sought so that observations from ICI and other microwave and sub-millimetre instruments can be used to their full potential to improve NWP, and by implication, climate models.

In this paper, we apply accelerated BEM [54, 55] to complex aggregates of rosettes to compute their SSPs between the size parameters of 0.005 and 71. The methods are implemented using the boundary element software Bempp (www.bempp.com) [75]. We consider 65 different model aggregates, of maximum dimension between 10 and $10000\mu m$, at frequencies of 50, 183, 243 and 664 GHz, and at temperatures of -83°C, -43°C, and -3°C. We note that the size parameter of 71 is not a limitation of the method. To compute the SSPs of non-spherical particles in the microwave and sub-millimetre regions it is necessary to assume differing temperatures because it is well-known that in those spectral regions, the complex refractive index of solid ice is temperature dependent [76, 6, 63]. Here, we choose to use the complex refractive index compilation of [76] for our single-scattering computations because it was the one recommended by [64].

The distinguishing feature between the compilation of SSPs presented here, and others is that we construct the rosette aggregates to follow mostly an observed mass-dimension relationship that is currently utilised in the cloud microphysics scheme of the Met Office's global Unified Model (UM). This ensures consistency between the UM cloud microphysics assumptions, and the SSPs used to simulate the microwave and sub-millimetre radiances that will be compared to the ICI measurements as part of the process of assimilating those observations. This consistency is also important for the retrieval of cloud ice properties from ICI measurements, as the amount of ice mass used in the radiative transfer simulations to mimic those radiance measurements will correspond to a commonly observed mass-dimension relation. This lack of consistency between an NWP model and SSPs used in simulations of microwave and sub-millimetre observations needs to be corrected for as found in the study by Fox [2] because the sub-millimetre region is particularly sensitive to the column integrated ice mass and the characteristic size of the

3

particle size distribution [4, 5].

The structure of the paper is as follows. In Section 2, the microphysical model is fully described, and comparisons are presented between the model's prediction of mass and orientation-averaged projected area to the mass- and area-dimension power laws that commonly occur in cirrus. In Section 3, we briefly discuss the scattering problem to be solved for, the BIE formulation used, and the far-field definitions of the SSPs that are derived in this paper are given. In Section 4, the treatment of three-dimensional random orientation is described, and this interpretation is tested against the T-matrix method developed for non-axisymmetric cylinders. Section 5 details the optimal mesh size, and the number of waves and polarisation directions required to ensure accurate BEM solutions found for the SSPs. Throughout this section, the optimal settings are tested against the corresponding T-matrix solutions obtained for a number of size parameters. Comparisons against alternative electromagnetic methods such as DDA are also discussed. A discussion of our findings and concluding remarks are provided in Section 6.

2. The microphysical model

The microphysics model is based on an in-situ analysis of Cloud Particle Imager (CPI) data from twenty-two campaigns distributed throughout the mid-latitudes, tropics, and southern latitudes analysed by Lawson *et al* [12]. The number of CPI images of ice crystal shapes numbered more than ten million. From the CPI images, the authors of [12] obtained representative distributions of ice crystal shapes within four differing ice cloud regimes. These regimes were in-situ generated cirrus, tropical maritime, tropical continental, and mid-latitude continental, where the latter three comprised anvils, and outflows from those anvils. From the CPI images, Lawson *et al* [12] were able to derive, for each of the regimes, representative mass– and area–dimension power laws. Here, we examine the shape distributions obtained from in-situ generated cirrus in particular, this is because this cloud type is common in the mid-latitudes, and we note the shape distribution for maximum dimensions greater than $100\mu m$. These larger sizes are more relevant to the microwave and sub-millimetre region of the electromagnetic spectrum.

From the analysis of [12], the most representative ice crystal shapes of relevance to modelling millimetre wave and sub-millimetre wave scattering found within in-situ generated cirrus are budding rosettes and aggregates of rosettes. We note further that the study also found that the rosettes contributed most to the observed mass and area distributions compiled from the in-situ generated cirrus. These are the two habits that are used here to compute the SSPs. However, the rosette aggregates are modelled to follow the Cotton *et al* [72] mass–dimension relationship, which is currently utilised in the cirrus microphysics scheme within the operational global UM used at the Met Office. The Cotton *et al* [72] mass-dimension relationship is quite general as it agrees with independent determinations of the mass-dimension relationship found by Heymsfield *et al* [70] and Erfani and Mitchell [73].

To model the rosettes, we utilise the ice aggregation model of Westbrook *et al* [69], whereby the aggregation process is simulated explicitly using a Monte Carlo model to sample collisions between particles falling at different speeds. The simulation begins with a population of monomer crystals, the shape of which can be chosen to match the observed monomer crystals in the cloud of interest. These particles collide and stick together to produce an ensemble of complex aggregates. These aggregates are formed by a collection kernel that considers the geometric cross sections for the collisions and the difference in fall speed between the realised ice crystals. Here, to form these ice crystals and aggregates, we consider budding rosettes and aggregates of rosettes. The monomer rosettes are constructed of three-branched rosettes, which are aggregated together to follow the Cotton *et al* [72] mass–dimension relationship given by

$$\text{mass} = 0.0257 D^2_{max}. \tag{1}$$

Each of the monomers that makes up the ensemble of rosette aggregates is assumed to have the density of solid ice, which has a value of $917\ kg/m^3$, and D_{max} is the maximum dimension of the ice crystal, where here it is defined as the maximum span of the two-dimensional projection of each ice crystal onto a plane. It is defined in this way as this is typically how the maximum dimension is determined using in-situ microphysics probes.

Multiple models were generated from the Monte Carlo realisations, and those that were within $\pm50\%$ of the Cotton *et al* [72] relationship were selected. The total number of model realisations selected was 65. The mass against D_{max} of the model selections are shown in Figure 1. The Monte Carlo generated ice aggregate model is shown to follow the Cotton *et al* [72] relationship correctly for sizes greater than approximately $500\mu m$. In fact, most of the rosette aggregates are well within $\pm30\%$ of the Cotton *et al* [72] relationship for maximum dimensions greater than $492\mu m$. At maximum dimensions less than this, the model aggregate at $492\mu m$ is scaled down to all other maximum dimensions. Therefore, at approximately $500\mu m$, there is a transition between the mass of the rosette aggregate varying as D^3_{max} and D^2_{max} for sizes less than or greater than approximately $500\mu m$, respectively. Also plotted in Figure 1 are the in-situ regime mass–dimension results derived by Lawson *et al* [12], and rather interestingly, the Cotton *et al* [72] relationship has a gradient that differs to this. Nonetheless, because the rosette aggregate model used here is based on the in-situ generated cirrus observations, this model is generally fairly close to the in-situ generated cirrus predicted masses for maximum dimensions that are less than approximately $2000\mu m$. For maximum dimensions greater than this, the Cotton *et al* [72] relationship predicts ice masses that are somewhat lower than the
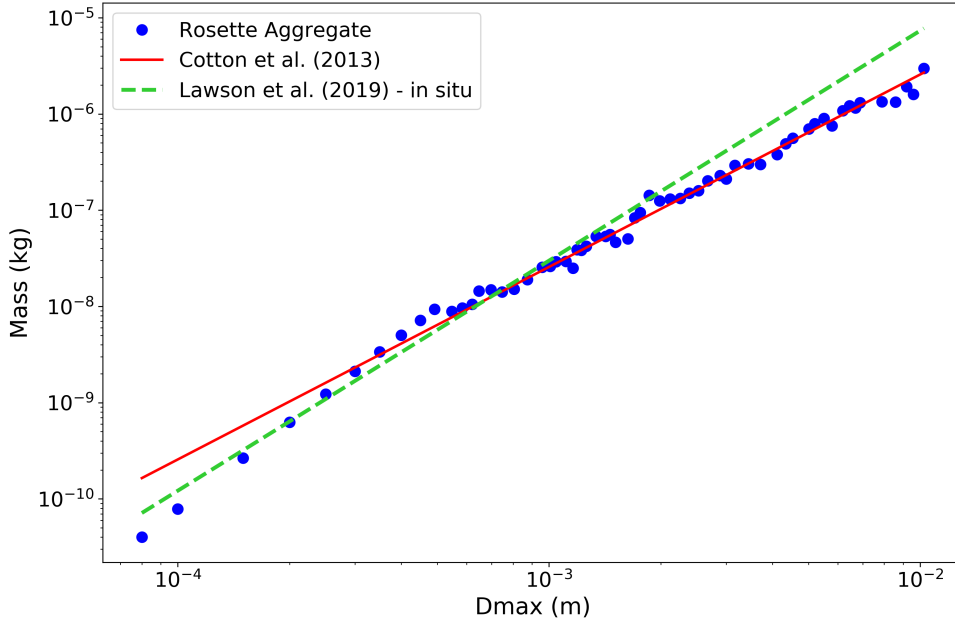
4

Figure 1: Mass of ice crystals plotted against the maximum dimension, showing the in-situ (dashed green line) regime mass-dimension relationship as derived by Lawson *et al* [12]. Compared against this relationship are the rosette aggregate model (filled blue circles), and the Cotton *et al* [72] relationship (red line).

predicted in-situ generated ice masses. This note exemplifies the importance of millimetre wave and sub-millimetre wave observations in providing data that can be used to potentially discriminate between differing mass–dimension relationships. Moreover, it should be further stated that the Lawson *et al* [12] analysis is limited to a maximum dimension of approximately $1000\mu m$ or less. Further mass and area data are required for maximum dimensions much greater than this to test model predictions over a much greater range of maximum dimensions than is presently provided.

Given that Figure 1 shows how well the rosette aggregate models follow the Cotton *et al* [72] mass–dimension relationship, in Figure 2 we investigate how well they follow the Lawson *et al* [12] in-situ generated cirrus area–dimension relationship. The projected areas of the rosette aggregates are calculated from the area ratios that are provided from within the Westbrook *et al* [69] ice aggregation model. In that model, the rosette aggregates are randomly re-oriented, the calculation of the area ratio is repeated in the $x - y$ plane N times the random re-orientation for each repeat. To compute the area ratio, the projected area is computed in the $x - y$ plane of the rosette aggregate divided by $(\pi * D_{max}^2/4)$. To compute the area ratio we divide the projected area of the non-spherical particle by the maximum possible projected area of a sphere of the same D_{max} as the non-spherical particle. From the area ratio, the orientation-projected

area of the rosette aggregates can be readily computed. As the aggregate model is oriented over a number of realisations, here it is ten orientations to obtain the mean and standard deviation at each maximum dimension. Ten realisations are sufficient to obtain the projected areas to within an accuracy of approximately 2%.

The means and standard deviations of all the rosette aggregate orientation-averaged area values are presented in Figure 2, along with the Lawson *et al* [12] in-situ generated cirrus area–dimension relationship and the Vouk [77] relationship. The use of the Vouk [77] relationship is to verify the computation of the orientation-averaged projected area from the ice aggregation model by computing the surface areas of the rosette aggregates, which are convex particles. The orientation-averaged projected area, denoted by $\langle P \rangle$, can be calculated from the surface area S of a convex particle using the equation $\langle P \rangle = S/4$. The surface area S is computed using standard formulae for the hexagonal prism and hexagonal pyramid, with the area of the top base of the hexagonal prism meeting the bottom base of the hexagonal pyramid subtracted because this area will be "hidden" in projection.

Figure 2 shows that the rosette aggregate model follows the Lawson *et al* [12] area–dimension relationship determined from the in-situ generated cirrus data rather well, where the in-situ determination of averaged area is within the standard deviations of the model up to approximately $5000\mu m$. However, there should also be an uncertainty
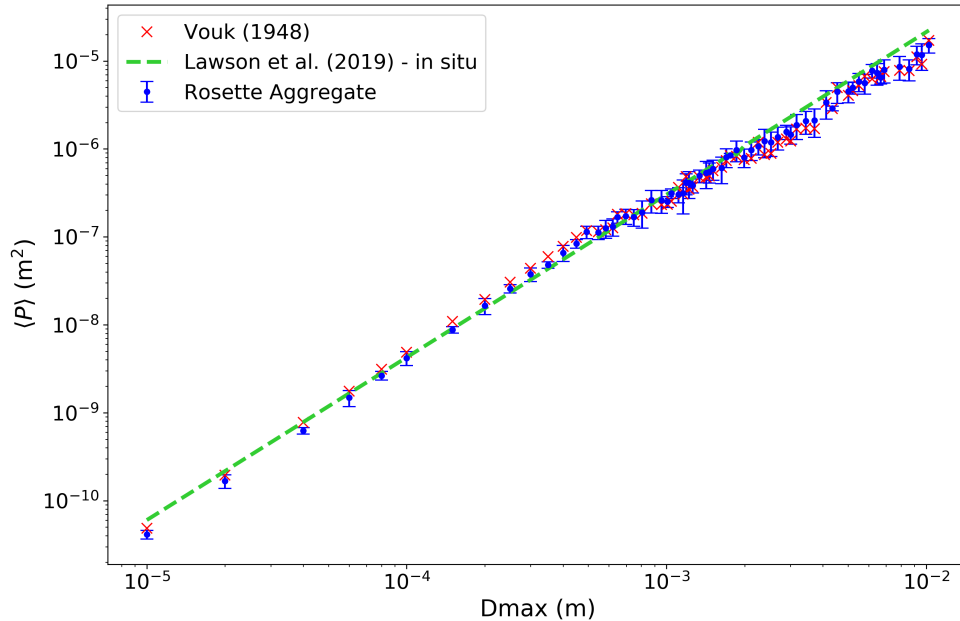
Figure 2: The orientation-averaged area, $\langle P \rangle$, plotted against the maximum dimension showing the Lawson *et al* [12] area determination obtained from in-situ generated cirrus (dashed green line), and the rosette aggregate model (blue standard deviations). The red cross symbols are the $\langle P \rangle$ values of the rosette aggregate model using the Vouk [77] relationship.

associated with the in-situ data. This is not presently known, but an uncertainty value of $\pm 50\%$ is normal for the in-situ estimation of the projected area of ice crystals [78]. Moreover, the Vouk relationship at maximum dimensions greater than approximately $492\mu m$ is also generally well within the standard deviation of the model, thus verifying the computation of orientation-averaged projected areas from the ice aggregation model.

Figure 3 shows the rosette aggregate geometrical properties expressed as power laws in terms of relationships between the ice crystal maximum dimension and the surface area, and volume, respectively. As expected, the fractal dimension of the rosette aggregate surface area has a value of 2 for maximum dimensions less than $492\mu m$, and 1.64, as the particles become elongated at maximum dimension values greater than $492\mu m$. In the case of the volume property, the rosette aggregate has a fractal dimension of 3.0 at sizes less than $492\mu m$, which decreases down to 1.94 at maximum dimensions greater than $492\mu m$, as shown in Figure 3.

Figures 4 - 7 show images of the ice aggregate models from Figure 1 that are used to generate the single-scattering properties. The meshing software Gmsh [79] was used to generate the meshes of the aggregate models. The figures shows the variation in the differing Monte Carlo realisations of the budding and rosette aggregate models, and no two adjacent models are exactly the same, except for $D_{max} = 10 - 492\mu m$. As such, we should not ex-

pect the SSPs to necessarily vary smoothly from one model to another. The aggregates consist of 6 to 168 monomers of different complexity.

For the simulations that follow, we use the Mätzler [76] compilation of ice refractive index. The choice of refractive indices to use in the microwave region was studied in detail by Eriksson *et al.* [6]. In the paper the authors concluded that Mätzler [76] was a good choice of refractive index to use in the microwave region, up to 1 THz for the range of atmospheric temperatures encountered in the Earth's atmosphere. More recently, Eriksson *et al.* [64] also commented upon this choice. They too came to the same conclusion as their earlier paper. Moreover, the latter paper states that newer refractive index models, such as Iwabuchi and Yang [80] and Warren and Brandt [81], are essentially identical to the compilation of Mätzler [76]. The database of Eriksson *et al.* [64] is based on the Mätzler [76] compilation. For these reasons, we too chose the Mätzler [76] compilation for our computations to be consistent with the Eriksson *et al.* [64] database.

3. The scattering problem and BEM

We treat each budding rosette/rosette aggregate as a multi-particle configuration with each individual monomer representing an individual scatterer. This is to take advantage of accelerating methods from [54, 82, 55] suitable for multi-particle scattering set ups. To ensure Lipschitz continuity of the boundary, Groth *et al* [52] have introduced
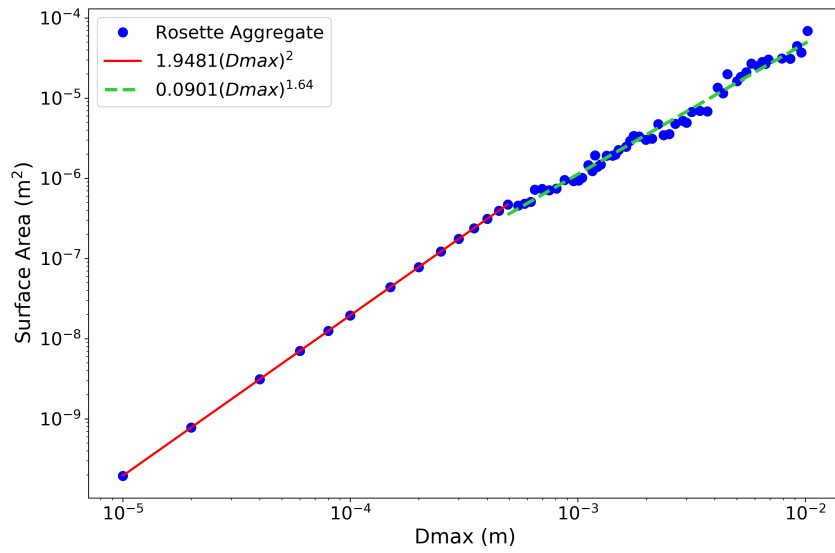
(a)
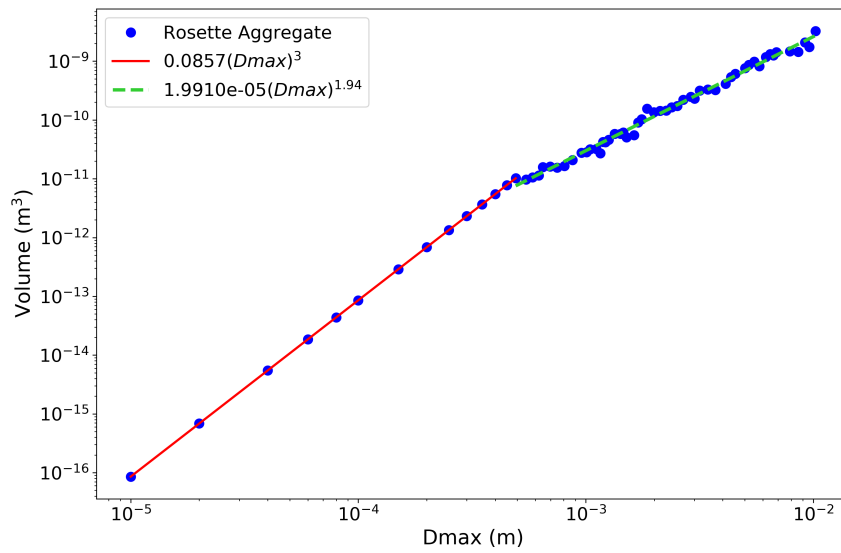
(b)

Figure 3: Rosette aggregate's surface area (a) and Volume (b) as a function of the maximum dimension. The power law fits are also shown for particles of $D_{max} < 492 \mu m$ and $\geq 492 \mu m$.

$D_{max} = 10 - 492\mu m$

$D_{max} = 547\mu m$

$D_{max} = 584\mu m$

$D_{max} = 621\mu m$

$D_{max} = 647\mu m$

$D_{max} = 697\mu m$

$D_{max} = 748\mu m$

$D_{max} = 805\mu m$

$D_{max} = 875\mu m$

$D_{max} = 958\mu m$

$D_{max} = 1008\mu m$

$D_{max} = 1045\mu m$

$D_{max} = 1111\mu m$

$D_{max} = 1160\mu m$

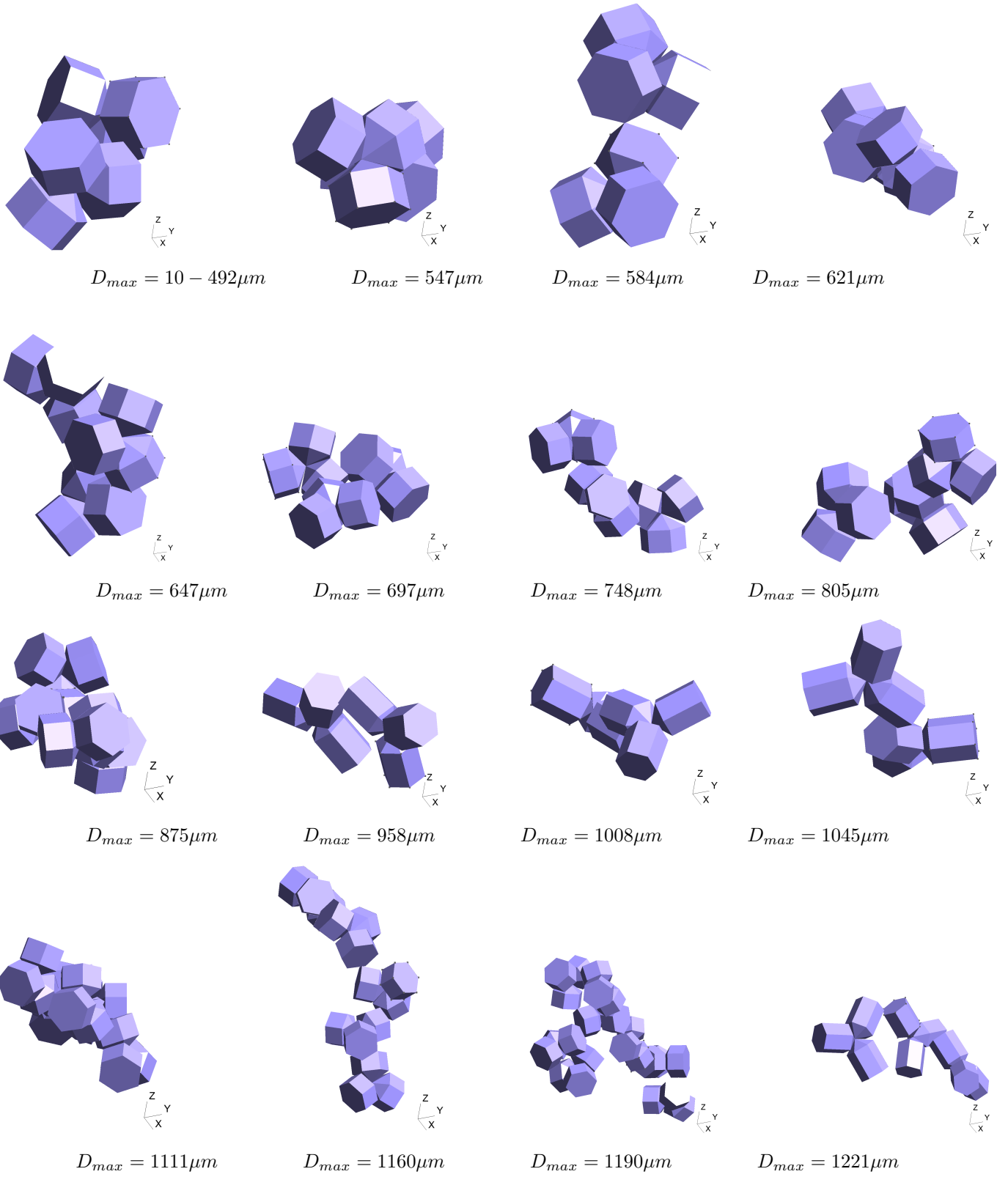$D_{max} = 1190\mu m$

$D_{max} = 1221\mu m$

Figure 4: Images of the budding rosettes and ice aggregate models used to generate the scattering database. The models are shown as a function of increasing maximum dimension, D_{max}, from 10 to 1221 μm.
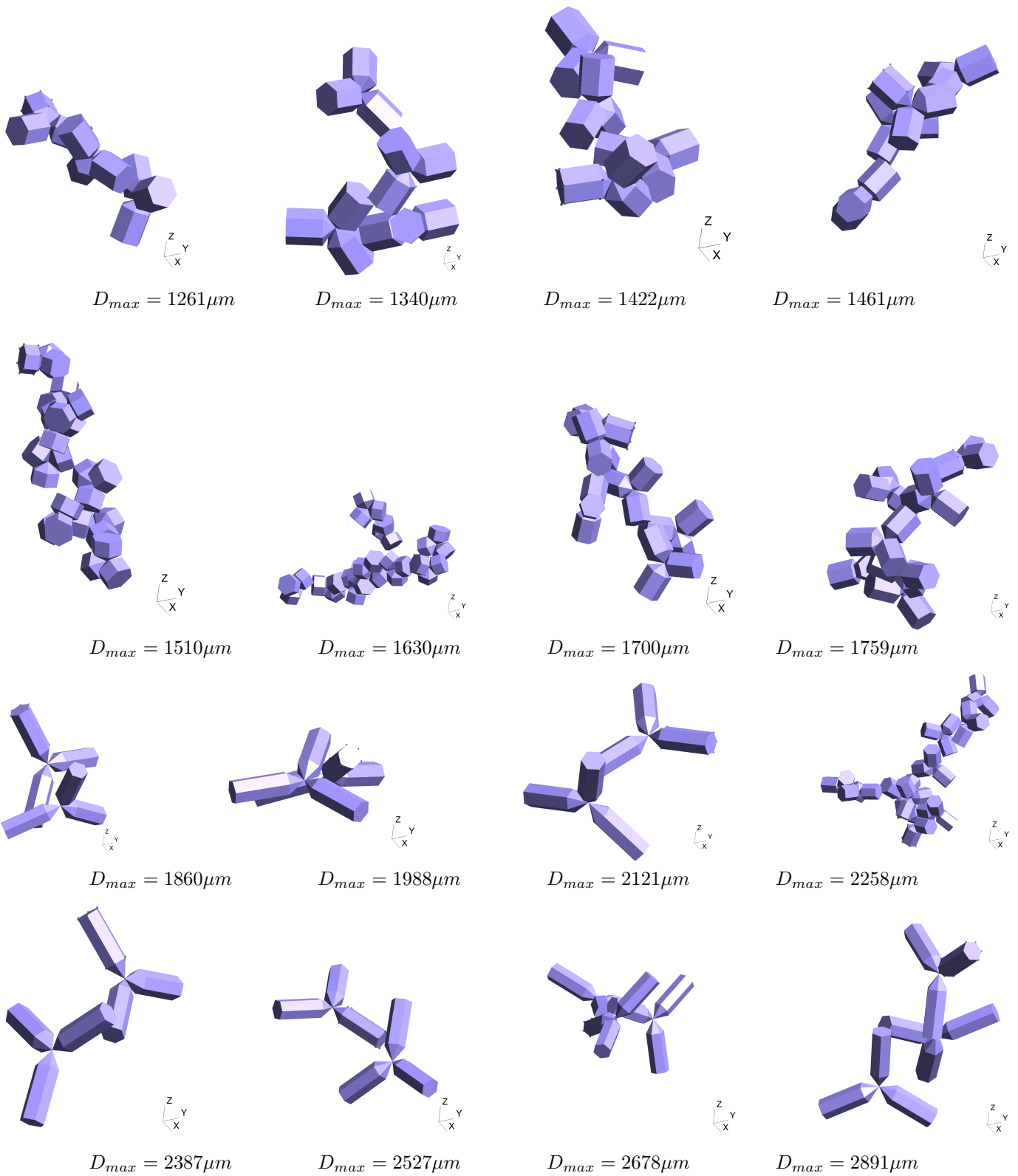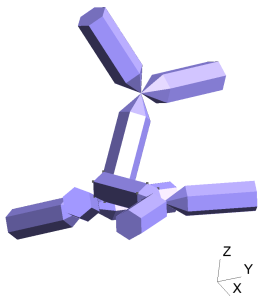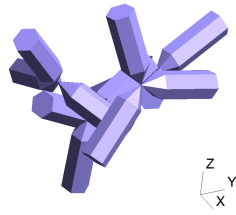
$D_{max} = 1261\mu m$ $D_{max} = 1340\mu m$ $D_{max} = 1422\mu m$ $D_{max} = 1461\mu m$

$D_{max} = 1510\mu m$ $D_{max} = 1630\mu m$ $D_{max} = 1700\mu m$ $D_{max} = 1759\mu m$

$D_{max} = 1860\mu m$ $D_{max} = 1988\mu m$ $D_{max} = 2121\mu m$ $D_{max} = 2258\mu m$

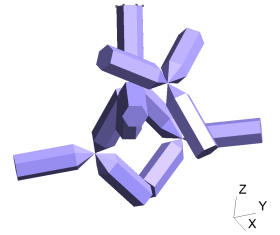$D_{max} = 2387\mu m$ $D_{max} = 2527\mu m$ $D_{max} = 2678\mu m$ $D_{max} = 2891\mu m$

Figure 5: Same as in Figure 4 but for D_{max} from 1261 to 2891 μm.
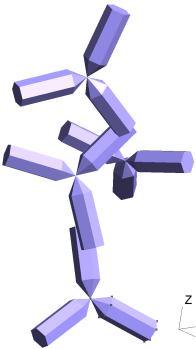
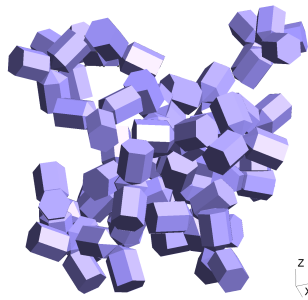9

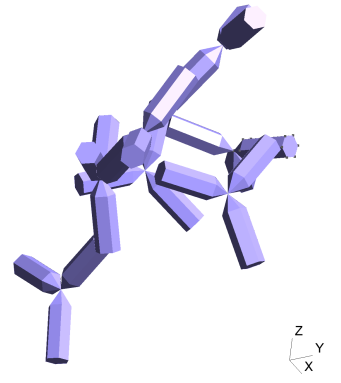$D_{max} = 3004\mu m$ $D_{max} = 3170\mu m$ $D_{max} = 3443\mu m$

$D_{max} = 3711\mu m$ $D_{max} = 4115\mu m$ $D_{max} = 4346\mu m$

$D_{max} = 4539\mu m$ $D_{max} = 5009\mu m$ $D_{max} = 5203\mu m$

$D_{max} = 5508\mu m$ $D_{max} = 5791\mu m$ $D_{max} = 6188\mu m$

Figure 6: Same as in Figure 4 but for D_{max} from 3004 to 6188 μm.

10

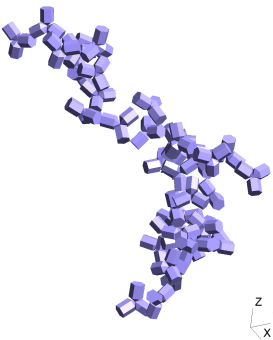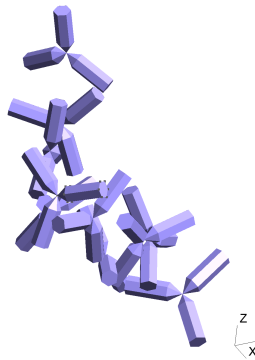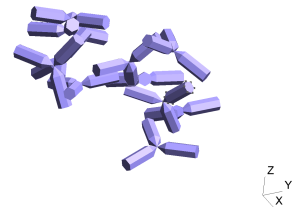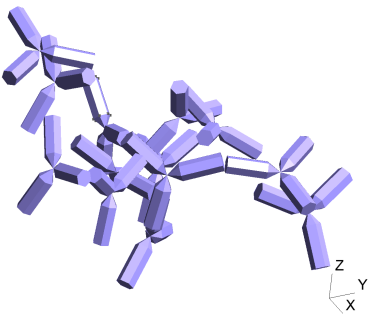$D_{max} = 6456\mu m$ $D_{max} = 6688\mu m$ $D_{max} = 6881\mu m$
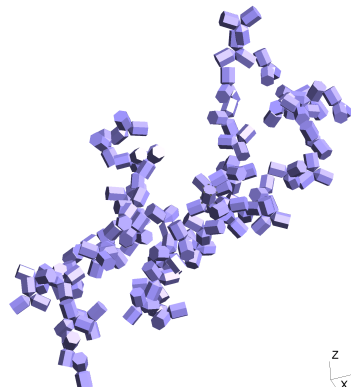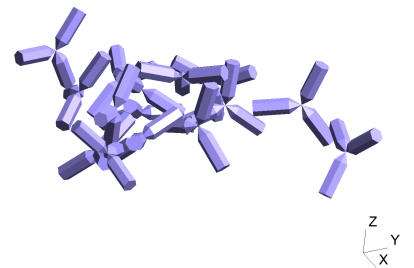
$D_{max} = 7884\mu m$ $D_{max} = 8582\mu m$ $D_{max} = 9200\mu m$

$D_{max} = 9594\mu m$ $D_{max} = 10235\mu m$

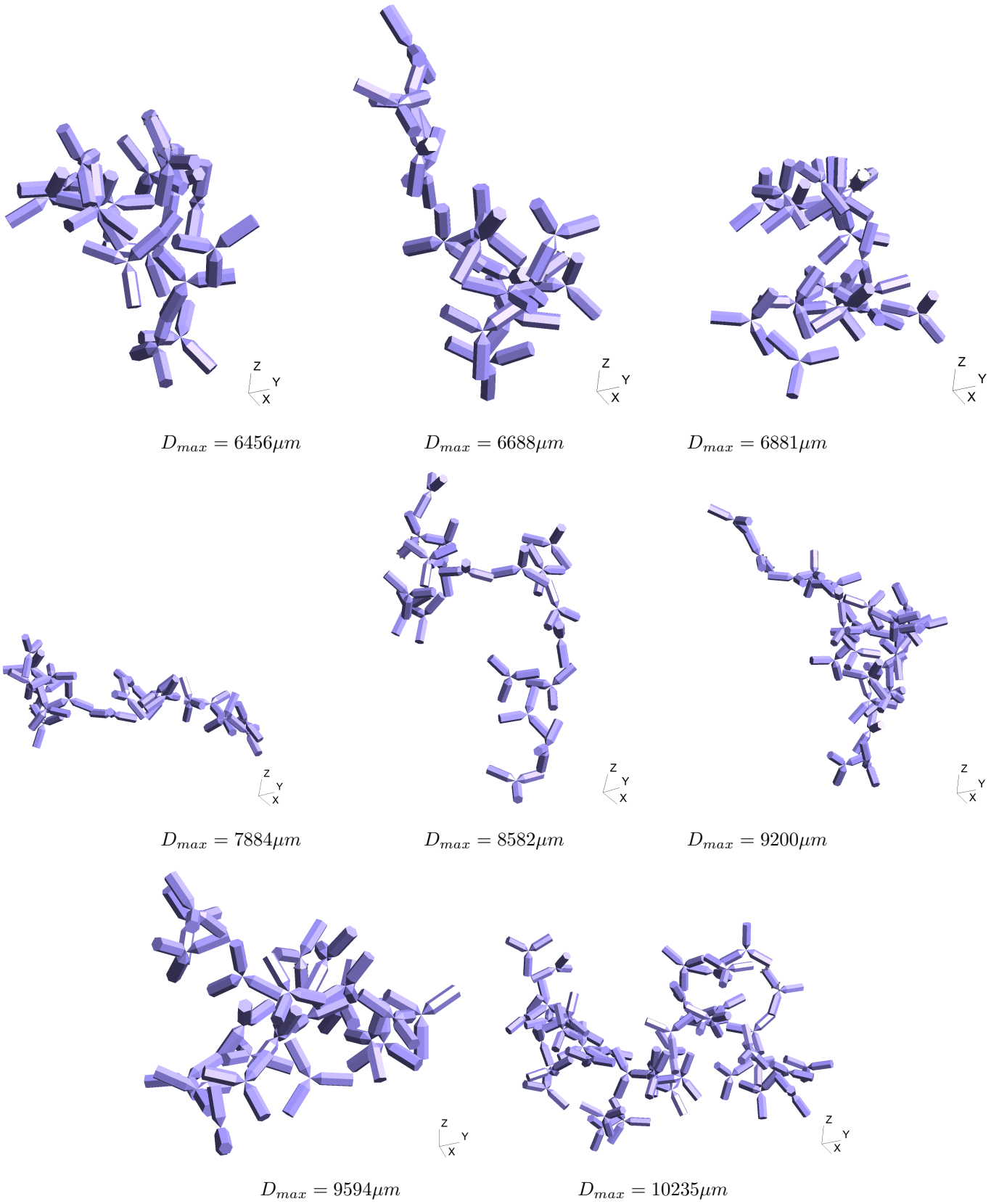Figure 7: Same as in Figure 4 but for D_{max} from 6456 to 10235 μm.

Temp	50 GHz	183 GHz	243 GHz	664 GHz
−83	1.7643 + 0.00042i	1.7643 + 0.00154i	1.7643 + 0.00207i	1.7643 + 0.00649i
−43	1.7746 + 0.00064i	1.7746 + 0.00235i	1.7746 + 0.00314i	1.7746 + 0.00940i
−3	1.7848 + 0.00120i	1.7849 + 0.00442i	1.7849 + 0.00589i	1.7849 + 0.01690i

Table 1: Complex refractive index for the three temperatures (°C), at the four different frequencies from [76].

small cubes (negligible compared to the size of the aggregate) where branches of bullet rosettes meet and treated the resulting aggregate as a single scatterer. Numerical experiments comparing the scattering properties confirmed that the introduction of the cube made a negligible difference. Theoretical results from [83, 84] show that one can also treat each monomer as an individual scatterer by studying the validity of the formulation as the separation between scatterers approaches 0. Numerical experiments from [54, 82, 55] have confirmed that these theoretical results also hold true using our implementation.

The scattering problem can then be described as a 3D time-harmonic electromagnetic scattering problem (with $e^{-i\omega t}$) by M disjoint isotropic homogeneous (but not necessarily identical) dielectric scatterers occupying bounded domains $\Omega_m^i \subset \mathbb{R}^3$, $m = 1, \ldots, M$, with boundaries $\Gamma_m = \partial\Omega_m^i$, in a homogeneous exterior medium $\Omega^e = \mathbb{R}^3 \backslash \cup_{m=1}^M \Omega_m^i$. The electric permittivity and magnetic permeability of scatterer Ω_m^i is denoted by ϵ_m and μ_m respectively, with the resulting wavenumber $k_e = \omega\sqrt{\mu_m\epsilon_m}$. The corresponding parameters for Ω^e are ϵ_e, μ_e and $k_e = \omega\sqrt{\mu_e\epsilon_e}$. The refractive index of Ω_m^i is denoted by n_m. For the purposes considered here, the magnetic permeabilities have the associated values for ice, i.e. $\mu_e = \mu_m = 1$, for $m = 1, \ldots, M$, and the refractive indices at different temperatures are taken from [76] and shown in Table 1.

An incident field $(\mathbf{E}^{inc}, \mathbf{H}^{inc})$ in Ω^e gives rise to interior fields $(\mathbf{E}_m^i, \mathbf{H}^{inc})$ in Ω_m^i, for $m = 1, \ldots, M$, and a scattered field $(\mathbf{E}^s, \mathbf{H}^s)$ in Ω^e, which is assumed to satisfy the Silver-Müller radiation condition. The total exterior field $(\mathbf{E}^e, \mathbf{H}^e)$ is the sum of the incident and scattered field

$$\mathbf{E}^e = \mathbf{E}^{inc} + \mathbf{E}^s, \tag{2}$$

$$\mathbf{H}^e = \mathbf{H}^{inc} + \mathbf{H}^s, \quad \text{in } \Omega^e. \tag{3}$$

The interior and exterior fields are assumed to satisfy the time-harmonic Maxwell equations

$$\nabla \times \mathbf{E}_m^i = i\omega\mu_m\mathbf{H}_m^i, \tag{4}$$

$$\nabla \times \mathbf{H}_m^i = -i\omega\epsilon_m\mathbf{E}_m^i, \quad \text{in } \Omega_m^i, \tag{5}$$

and

$$\nabla \times \mathbf{E}^e = i\omega\mu_e\mathbf{H}^e, \tag{6}$$

$$\nabla \times \mathbf{H}^e = -i\omega\epsilon_e\mathbf{E}^e, \quad \text{in } \Omega^e, \tag{7}$$

with the transmission boundary conditions

$$\mathbf{E}_m^i(\mathbf{r}) \times \mathbf{n}_m = \mathbf{E}^e(\mathbf{r}) \times \mathbf{n}_m, \tag{8}$$

$$\mathbf{H}_m^i(\mathbf{r}) \times \mathbf{n}_m = \mathbf{H}^e(\mathbf{r}) \times \mathbf{n}_m, \tag{9}$$

for $\mathbf{r} \in \Gamma_m$, $m = 1, \ldots, M$. Here $\mathbf{n}_m$ is the outgoing unit normal vector on Γ_m. It is sufficient to solve for the electric fields alone (as we do for the purposes of this paper), and recover the magnetic fields. The electric fields satisfy

$$\nabla \times (\nabla \times \mathbf{E}_m^i) - k_m^2\mathbf{E}_m^i = 0, \text{ in } \Omega_m^i, \tag{10}$$

$$\nabla \times (\nabla \times \mathbf{E}^e) - k_e^2\mathbf{E}^e = 0, \text{ in } \Omega^e. \tag{11}$$

3.1. The PMCHWT formulation

The PMCHWT formulation (due to Poggio, Miller, Chang, Harrington, Wu and Tsai [44, 45, 46, 47]) is used to transform the electromagnetic scattering problem from PDEs to boundary integral equations here. We refer the reader to [54, 55] for details on the PMCHWT formulation in the multi-particle setting and for further details, including a discussion of the function space setting, we refer to [85].

3.2. Galerkin discretisation and accelerated Calderón preconditioning

Galerkin discretisation of the PMCHWT formulation is used to transform the BIEs into a matrix system but this leads to an ill-conditioned linear system requiring large number of iterations to be solved by GMRES [86] (and other iterative solvers in general). Calderón preconditioning [48, 49, 50, 51], an operator-based approach [56], is used to remedy this but this comes with additional costs. To obtain a stable discretisation of the operator products that arise in this approach, the use of a dual mesh defined on a barycentrically refined grid (hence increasing memory costs) needs to be considered [57]. In addition, to capture the oscillatory solution of the electromagnetic waves, the mesh needs to be refined with respect to frequency [52], making the simulation of high-frequency problems, such as the ones considered here, very expensive.

To alleviate the additional costs the accelerating techniques of [54, 55] have been employed here, as they have demonstrated a reduction by 99% in memory costs and 80% in total computation time for the high frequency problems considered (at frequency 664 GHz and size parameter
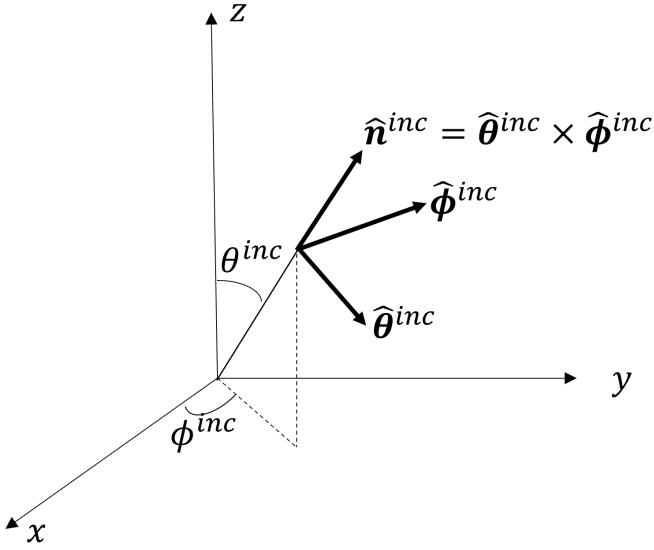
Figure 8: Scattering set up for the incident wave. The angles $(\theta^{inc}, \phi^{inc})$ are the polar (zenith) and azimuth angles respectively and satisfy $\theta^{inc} \in [0, \pi]$ and $\phi^{inc} \in [0, 2\pi]$. A similar coordinate system $(\hat{\mathbf{n}}^{sca}, \hat{\boldsymbol{\theta}}^{sca}, \hat{\boldsymbol{\phi}}^{sca})$ can be defined to describe the scattered wave.

70). The accelerating techniques were based on a combination of modifying the preconditioning operators, a bi-parametric implementation and treatment of the resulting aggregate as a multi-particle problem rather than a single-particle one. For a full description of the preconditioners, discretisation of the operator product and the bi-parametric assembly we direct the reader to [54, 55].

3.3. Scattering in the far-field zone

To simulate the optical properties and phase matrix elements of the scattering problem knowledge of the far-field is required, with the far-field zone being the area where $k_e r \gg 1$ [87]. Before we proceed to define the scattered far-field and its properties we fix some notation.

A spherical coordinate system can be employed to describe the scattering setup as seen in Figure 8, with the direction of propagation of the incident plane electromagnetic wave defined by $\hat{\mathbf{n}}^{inc}$ and corresponding unit vectors $\hat{\boldsymbol{\theta}}^{inc}$ and $\hat{\boldsymbol{\phi}}^{inc}$ such that $\hat{\mathbf{n}}^{inc} = \hat{\boldsymbol{\theta}}^{inc} \times \hat{\boldsymbol{\phi}}^{inc}$ and defined as

$$\hat{\mathbf{n}}^{inc} = \begin{bmatrix} \sin\theta^{inc}\cos\phi^{inc} \\ \sin\theta^{inc}\sin\phi^{inc} \\ \cos\theta^{inc} \end{bmatrix},$$

$$\hat{\boldsymbol{\theta}}^{inc} = \begin{bmatrix} \cos\theta^{inc}\cos\phi^{inc} \\ \cos\theta^{inc}\sin\phi^{inc} \\ -\sin\theta^{inc} \end{bmatrix},$$

$$\hat{\boldsymbol{\phi}}^{inc} = \begin{bmatrix} -\sin\phi^{inc} \\ \cos\phi^{inc} \\ 0 \end{bmatrix}. \quad (12)$$

Since the medium of propagation is assumed to be non-absorbing, the component of the electric field vector along

the direction of propagation $\hat{\mathbf{n}}^{inc}$ is zero and the incident field can then be decomposed into components in the $\hat{\boldsymbol{\theta}}^{inc}$ and $\hat{\boldsymbol{\phi}}^{inc}$ directions as follows

$$\mathbf{E}^{inc} = (E_\theta^{inc}\hat{\boldsymbol{\theta}}^{inc} + E_\phi^{inc}\hat{\boldsymbol{\phi}}^{inc})\exp(ik_e\hat{\mathbf{n}}^{inc} \cdot \mathbf{r}), \quad (13)$$

where $E_\theta^{inc}\hat{\boldsymbol{\theta}}^{inc}$ and $E_\phi^{inc}\hat{\boldsymbol{\phi}}^{inc}$ define the polarisation vectors. In the same manner, a coordinate system defined by $\hat{\mathbf{n}}^{sca}, \hat{\boldsymbol{\theta}}^{sca}, \hat{\boldsymbol{\phi}}^{sca}$ is used to describe the scattered wave.

The scattered far-field, $\mathbf{E}^{s,f}$, decays inversely with distance r from the scattering object

$$\mathbf{E}^{s,f}(\hat{\mathbf{n}}^{sca}) \sim \frac{e^{ik_e r}}{r}\mathbf{F}(\hat{\mathbf{n}}^{sca}), \quad r \to \infty. \quad (14)$$

The vector $\mathbf{F}$ is independent of r and describes the angular distribution of the scattered field radiation in the far-field zone. It can be computed via the asymptotic form of the Stratton Chu representation formulae

$$\mathbf{F}(\mathbf{x}) = -\sum_m^M \mathcal{H}_m^{e,f}\left(\gamma_{D,m}^+ \mathbf{E}_m^s\right) - \sum_m^M \mathcal{E}_m^{e,f}\left(\gamma_{N,m}^+ \mathbf{E}_m^s\right), \quad (15)$$

where $\mathcal{H}^{e,f}$ and $\mathcal{E}^{e,f}$ are the far-field versions of the magnetic and electric potential operators given as [52]

$$\mathcal{H}^{e,f}\mathbf{v}(\mathbf{x}) := \frac{ik_e}{4\pi}\int_\Gamma \exp\left(\frac{-ik_e\mathbf{x}\cdot\mathbf{y}}{|\mathbf{x}|}\right)\left(\frac{\mathbf{x}}{|\mathbf{x}|}\times\mathbf{v}(\mathbf{y})\right)d\Gamma(\mathbf{y}), \quad (16)$$

$$\mathcal{E}^{e,f}\mathbf{v}(\mathbf{x}) := \frac{ik_e}{4\pi}\int_\Gamma \exp\left(\frac{-ik_e\mathbf{x}\cdot\mathbf{y}}{|\mathbf{x}|}\right)\mathbf{v}(\mathbf{y})d\Gamma(\mathbf{y})$$
$$- \frac{ik_e}{4\pi}\int_\Gamma \exp\left(\frac{-ik_e\mathbf{x}\cdot\mathbf{y}}{|\mathbf{x}|}\right)\mathbf{v}(\mathbf{y})\cdot\frac{\mathbf{x}}{|\mathbf{x}|}d\Gamma(\mathbf{y}), \quad (17)$$

and $\gamma_{D,m}^+$ and $\gamma_{N,m}^+$ are the exterior Dirichlet and Neumann traces for which we refer the reader to [85].

3.4. Amplitude Scattering Matrix

The elements of the amplitude matrix $\mathbf{S}$ are expressed as follows [87]

$$S_{11} = \hat{\boldsymbol{\theta}}^{sca} \cdot \mathbf{F}^{s,f}(\hat{\mathbf{n}}^{sca}, \hat{\mathbf{n}}^{inc}, \hat{\boldsymbol{\theta}}^{inc}), \quad (18)$$

$$S_{12} = \hat{\boldsymbol{\theta}}^{sca} \cdot \mathbf{F}^{s,f}(\hat{\mathbf{n}}^{sca}, \hat{\mathbf{n}}^{inc}, \hat{\boldsymbol{\phi}}^{inc}), \quad (19)$$

$$S_{21} = \hat{\boldsymbol{\phi}}^{sca} \cdot \mathbf{F}^{s,f}(\hat{\mathbf{n}}^{sca}, \hat{\mathbf{n}}^{inc}, \hat{\boldsymbol{\theta}}^{inc}), \quad (20)$$

$$S_{22} = \hat{\boldsymbol{\phi}}^{sca} \cdot \mathbf{F}^{s,f}(\hat{\mathbf{n}}^{sca}, \hat{\mathbf{n}}^{inc}, \hat{\boldsymbol{\phi}}^{inc}). \quad (21)$$

By $\mathbf{F}^{s,f}(\hat{\mathbf{n}}^{sca}, \hat{\mathbf{n}}^{inc}, \hat{\boldsymbol{\theta}}^{inc})$ we mean the scattered far-field created by the $\hat{\boldsymbol{\theta}}^{inc}$ component of the incident plane wave, i.e. $E_\theta^{inc}\hat{\boldsymbol{\theta}}^{inc}\exp(ik_e\hat{\mathbf{n}}^{inc}\cdot\mathbf{r})$ and evaluated in the scattering direction $\hat{\mathbf{n}}^{sca}$. Analogous definitions can be made for $\mathbf{F}^{s,f}(\hat{\mathbf{n}}^{sca}, \hat{\mathbf{n}}^{inc}, \hat{\boldsymbol{\phi}}^{inc})$.

3.5. Phase matrix

The elements of the phase matrix, **Z**, that are relevant for this article are as follows [87]

$$Z_{11} = \frac{1}{2} \left(|S_{11}|^2 + |S_{12}|^2 + |S_{21}|^2 + |S_{22}|^2 \right), \qquad (22)$$

$$Z_{12} = \frac{1}{2} \left(|S_{11}|^2 - |S_{12}|^2 + |S_{21}|^2 - |S_{22}|^2 \right), \qquad (23)$$

$$Z_{21} = \frac{1}{2} \left(|S_{11}|^2 + |S_{12}|^2 - |S_{21}|^2 - |S_{22}|^2 \right), \qquad (24)$$

$$Z_{22} = \frac{1}{2} \left(|S_{11}|^2 - |S_{12}|^2 - |S_{21}|^2 + |S_{22}|^2 \right), \qquad (25)$$

$$Z_{33} = \Re \left(S_{11} S_{22}^* + S_{12} S_{21}^* \right), \qquad (26)$$

$$Z_{34} = \Im \left(S_{11} S_{22}^* + S_{21} S_{12}^* \right), \qquad (27)$$

$$Z_{43} = \Im \left(S_{22} S_{11}^* - S_{12} S_{21}^* \right), \qquad (28)$$

$$Z_{44} = \Re \left(S_{22} S_{11}^* - S_{12} S_{21}^* \right), \qquad (29)$$

where $\Re$ and $\Im$ denote the real and imaginary parts respectively.

3.6. The total optical properties

Knowledge of the scattered far-field allows us to compute the total optical properties of the scatterer. These are the extinction, scattering and back-scattering cross sections, the asymmetry parameter and the single-scattering albedo, denoted by C_{ext}, C_{sca}, C_{bsca}, g and ϖ_0 respectively. The extinction, scattering and back-scattering cross sections can be computed as follows:

$$C_{ext} = \frac{1}{2} \left(C_{ext,\theta} + C_{ext,\phi} \right), \qquad (30)$$

$$C_{sca} = \frac{1}{2} \left(C_{sca,\theta} + C_{sca,\phi} \right), \qquad (31)$$

$$C_{bsca} = 4\pi Z_{11}(\theta^{sca} = \pi), \qquad (32)$$

where the individual $\hat{\boldsymbol{\theta}}$ and $\hat{\boldsymbol{\phi}}$ components can be computed by

$$C_{ext,x} = \frac{4\pi}{k_e |E_x^{inc} \hat{\boldsymbol{x}}^{inc}|^2} \Im \left(\mathbf{F}^{s,f}(\hat{\mathbf{n}}^{sca}, \hat{\mathbf{n}}^{inc}, \hat{\boldsymbol{x}}^{inc}) \cdot \left(E_x^{inc} \hat{\boldsymbol{x}}^{inc} \right)^* \right), \qquad (33)$$

$$C_{sca,x} = \frac{1}{|E_x^{inc} \hat{\boldsymbol{x}}^{inc}|^2} \int_{4\pi} |\mathbf{F}^{s,f}(\hat{\mathbf{r}}, \hat{\mathbf{n}}^{inc}, \hat{\boldsymbol{x}}^{inc})|^2 d\hat{\mathbf{r}}. \qquad (34)$$

The single-scattering albedo is defined as the ratio of the scattering and extinction cross sections

$$\varpi_0 = \frac{C_{sca}}{C_{ext}} \le 1. \qquad (35)$$

The asymmetry parameter, g, is defined as the average cosine of the scattering angle $\Theta = \arccos(\hat{\mathbf{r}} \cdot \hat{\mathbf{n}}^{inc})$, i.e. the angle between the incidence and the scattering directions

$$g = \langle \cos \Theta \rangle = \frac{1}{2} \left(g_\theta + g_\phi \right), \qquad (36)$$

where the individual components can be computed by

$$g_x = \frac{1}{C_{sca,x}} \int_{4\pi} |\mathbf{F}^{s,f}(\hat{\mathbf{r}}, \hat{\mathbf{n}}^{inc}, \hat{\boldsymbol{x}}^{inc})|^2 \hat{\mathbf{r}} \cdot \hat{\mathbf{n}}^{inc} d\hat{\mathbf{r}}. \qquad (37)$$

For the evaluation of any integrals over the sphere (i.e. for C_{sca} and g) we use Lebedev quadrature [88, 89, 90, 91, 92, 93]. This is to take advantage of the discrete grid points (θ_i, ϕ_i) being available as a pair and hence reducing the number of loops representing the integrals to one. Construction of the Lebedev grid points and weights can be tedius but we take advantage of pre-computed numerical values for the nodes and weights from [94]. We note that for the evaluation of C_{sca} and g we use Lebedev quadrature of order 59 resulting in 1202 grid points. We note that there are alternative ways of computing C_{sca} and g through the phase matrix element Z_{11} and the relative difference between the two definitions is used to check the accuracy of our implementation

4. Treatment of random orientation

Averaging some quantity f over random particle orientations is represented by [95]

$$\langle f \rangle = \frac{1}{8\pi^2} \int_0^{2\pi} \int_0^\pi \int_0^{2\pi} f(\alpha, \beta, \gamma) \sin \beta \, d\alpha \, d\beta \, d\gamma. \qquad (38)$$

The traditional approach to evaluate the SSPs and phase matrix of randomly oriented particles is to fix the direction of the incident wave, and then rotate the scatterer using three Euler angles α, β, γ (as described for example in [96] and seen in Figure 9). The rotation matrix representing the three rotations is given by

$$R_{\alpha\beta\gamma} = R_z(\gamma) R_y(\beta) R_z(\alpha), \qquad (39)$$

where

$$R_z(u) = \begin{bmatrix} \cos u & \sin u & 0 \\ -\sin u & \cos u & 0 \\ 0 & 0 & 1 \end{bmatrix}, \qquad (40)$$

$$R_y(u) = \begin{bmatrix} \cos u & 0 & -\sin u \\ 0 & 1 & 0 \\ \sin u & 0 & \cos u \end{bmatrix}. \qquad (41)$$

The SSPs and phase matrix are then evaluated for some scattering angles $(\theta^{sca}, \phi^{sca})$. Once many orientations have been considered one can use (38) to compute the orientationally averaged quantity.

A naive approach to this would be to re-assemble the PMCHWT operator and Calderón preconditioner (see earlier Section 3 and [54, 55] for more details) for each orientation considered, however this would be very expensive using BEM. Instead, two reference frames are often used when considering multiple orientations; a 'laboratory' reference frame and a particle one [87]. The laboratory frame is often chosen so that it corresponds to the geometry of
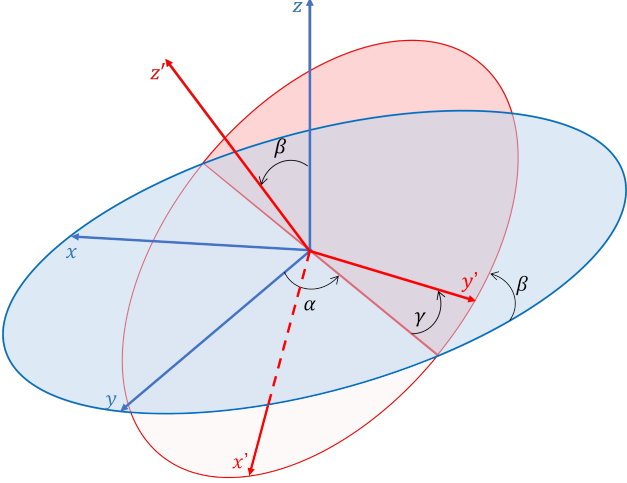
14

Figure 9: Euler angles α, β and γ transforming the original (blue) coordinate system xyz into a new one (red) $x'y'z'$.

the scattering situation, i.e., the Cartesian coordinate system. The particle reference frame is used to describe the orientation of the scatterer with respect to the laboratory frame. In order to solve the scattering problem with respect to the laboratory reference frame, one must first solve in the particle reference frame and then through suitable rotation matrices transition to the laboratory frame. Full details of this process and explicit formulas for the necessary rotation matrices are given in [87]. Fixing the direction of the incident wave and rotating the scatterer by $R_{\alpha\beta\gamma}$ is equivalent to fixing the orientation of the scatterer and instead rotating the direction of the incident wave by $R_{\alpha\beta\gamma}^{-1}$; and this methodology has also been considered in [97]. This enables us to assemble the operator matrix and preconditioner once and re-use for all incident wave solutions. We note that for each incident wave, two GMRES solves need to be performed; one for each polarisation vector as described in (12), but different GMRES solves can be distributed over different CPUs to reduce the total computational time.

Assuming a fixed incident wave direction with fixed $\theta^{inc} = \phi^{inc} = 0$ in (12), gives

$$\hat{\mathbf{n}}^{inc} = \begin{bmatrix} 0 \\ 0 \\ 1 \end{bmatrix}, \quad \hat{\boldsymbol{\theta}}^{inc} = \begin{bmatrix} 1 \\ 0 \\ 0 \end{bmatrix}, \quad \hat{\boldsymbol{\phi}}^{inc} = \begin{bmatrix} 0 \\ 1 \\ 0 \end{bmatrix}. \tag{42}$$

These can then be rotated by $R_{\alpha,\beta,\gamma}^{-1}$ given by

$$R_{\alpha,\beta,\gamma}^{-1} = R_z^{-1}(\alpha) R_y^{-1}(\beta) R_z^{-1}(\gamma), \tag{43}$$

giving the rotated incident directions and polarisation vec-

tors

$$\hat{\mathbf{n}}^{inc} = \begin{bmatrix} \cos\alpha\sin\beta \\ \sin\alpha\sin\beta \\ \cos\beta \end{bmatrix}, \tag{44}$$

$$\hat{\boldsymbol{\theta}}^{inc} = \begin{bmatrix} \cos\alpha\cos\beta\cos\gamma - \sin\alpha\sin\gamma \\ \sin\alpha\cos\beta\cos\gamma + \cos\alpha\sin\gamma \\ -\sin\beta\cos\gamma \end{bmatrix}, \tag{45}$$

$$\hat{\boldsymbol{\phi}}^{inc} = \begin{bmatrix} -\cos\alpha\cos\beta\sin\gamma - \sin\alpha\cos\gamma \\ -\sin\alpha\cos\beta\sin\gamma + \cos\alpha\cos\gamma \\ \sin\beta\sin\gamma \end{bmatrix}, \tag{46}$$

that can be varied for different α, β, γ. Comparing with the definitions of (12), we can see that both $\hat{\mathbf{n}}^{inc}$ are equivalent with $\alpha = \phi^{inc}$ and $\beta = \theta^{inc}$, i.e. the direction of the incident wave does not depend on the angle γ and can be defined using a pair of grid points $(\theta^{inc}, \phi^{inc})$. It is only the polarisation vectors $\hat{\boldsymbol{\theta}}^{inc}$ and $\hat{\boldsymbol{\phi}}^{inc}$ that need to be altered by an additional angle. This allows us to make use of Lebedev quadrature to obtain the grid points $(\theta_i^{inc}, \phi_i^{inc})$ that define the direction of the incident wave, reducing the two integrals over θ^{inc} and ϕ^{inc} (or α and β as defined in (38)) to just one. The third integral over γ can then be evaluated by a simple Gaussian integration. We therefore use the terms 'number of incident waves' to refer to the number of points obtained for $(\theta_i^{inc}, \phi_i^{inc})$ by the Lebedev scheme and 'number of polarisation vectors' to refer to the number of points γ_i obtained by the Gaussian quadrature scheme.

We also note that alternative ways to handle this exist in the literature. For example, in DDA simulations it is often used, that a rotation of polarisation (i.e. multiple γ_i values) is equivalent to the rotation of the scattering plane, i.e., it is sufficient to simulate two incident polarisations (one γ_i value). Once the matrix has been inverted, it may be applied to incident waves from different directions (equivalent to varying the orientation of the target, while keeping the incident direction constant)[98]. For further discussions on this we refer to [99] and references within. Regarding BEM, any information related to the incident wave (i.e. θ_i^{inc}, ϕ_i^{inc} or γ_i) will directly affect the right hand side of the discrete matrix system that needs to be solved. While a new right-hand side would in turn require a new GMRES solve, there are subspace recycling techniques that allow us to quickly iterate to the solution with another right-hand side if it does not deviate too much from the previous one. This option is not explored in this paper, but can be considered in the future. to accelerate convergence to the next solution.

4.1. Testing our implementation of random orientation

To test the accuracy of our implementation of random orientation as well as to find the number of incident waves and polarisation rotations that are needed to approximate random orientation, we compare with results obtained from a T-matrix method [20]. We consider scattering by

X	Dimensions	Frequency	Refractive Index
0.05	$L = D = 96\mu m$	50 GHz	$1.7746 + 0.00064i$
0.1	$L = D = 191\mu m$		
1	$L = D = 1.91mm$		
5	$L = D = 9.55mm$		
10	$L = D = 1.4mm$	664 GHz	$1.7746 + 0.00940i$

Table 2: Information on the geometry, frequency, refractive index for some of the test cases. The height of the hexagonal column is denoted by L, with the diameter of the hexagonal face by D.

hexagonal columns of different size parameters, X, as detailed in Table 2. The size parameter, X, is defined as

$$X = \frac{k_e D_{max}}{2}. \tag{47}$$

In Figure 10, we present the relative errors of SSPs computed for the problems of Table 2, for a number of incoming waves and for different mesh resolutions. We find that the prescribed mesh size of 10 elements per wavelength suggested in [52] is not a useful measure for all the hexagonal columns considered, as some are very small and require a refined mesh size to achieve a sufficient discretisation of the surfaces. In particular, this is the case for $X = 0.05$ and $X = 0.1$, as the maximum mesh size occurring from a rule of 10 elements per wavelength is larger than the length L of the columns, resulting in the minimum amount of elements per surface produced by Gmsh. A mesh size of 100 elements per wavelength was sufficient to reduce the relative errors to a few percent. We also observe that 14 incident waves in combination with the refined mesh are sufficient to provide accurate SSPs at a relative error of 1% or below, for size parameters $X = 0.05$ and 0.1. For size parameter $X = 1$, 14 waves and the usual 10 elements per wavelength are sufficient. A discretisation of 20 elements per wavelength increases accuracy but this is at the expense of computational time and memory consumption. For the hexagonal column of size parameter $X = 5$, we see that a mesh size of 10 elements per wavelength produces relative errors between 1-2%. A mesh size of 20 elements per wavelength reduces those relative errors below 1%. There is no obvious change in assuming 110 or 194 incident waves, except for a small increase in the relative error of $\langle C_{bsca} \rangle$ when 20 elements per wavelength are used. For the hexagonal column of size parameter $X = 10$, a mesh size of 10 elements per wavelength results in relative errors between 1-4%. These fall below 1% when a mesh of 20 elements per wavelength is used, except for $\langle g \rangle$ at 2% and $\langle C_{bsca} \rangle$ at 3%. Our numerical experiments show that the accuracy of the SSPs is not affected by varying γ; these can be computed accurately just by varying $(\theta^{inc}, \phi^{inc})$.

In Figures 11 - 12, we compare the phase matrix elements computed using our BEM against the T-matrix method of [20]. We note that the only elements of the phase matrix that remain non-zero when considering random orientation are $\langle Z_{11} \rangle$, $\langle Z_{22} \rangle$, $\langle Z_{33} \rangle$, $\langle Z_{44} \rangle$, $\langle Z_{12} \rangle$ ($= \langle Z_{21} \rangle$) and $\langle Z_{34} \rangle$ ($= -\langle Z_{43} \rangle$) and hence we only present comparisons for those. For the small size parameters $X = 0.05$ and $X = 1$ considered in Figure 11 we see a complete agreement between the methods with just 14 incident waves, in agreement with earlier findings on the accuracy of the integral optical properties. We note though that a different number of polarisation rotations had to be considered to achieve this accuracy; 5 for $X = 0.05$ and 10 for $X = 1$. For the larger size parameters $X = 5$ and $X = 10$ of Figure 12, 194 incident waves were considered for both cases, but 10 polarisation rotations for $X = 5$ and 15 for $X = 10$. A good agreement is observed between the BEM and T-matrix methods although not a complete match for some parts of $\langle Z_{11} \rangle$ and $\langle Z_{12} \rangle$. This could be remedied by using a finer mesh or by assuming a larger number of incident waves/polarisation rotations.

5. Accuracy of the SSPs

The question now arises as to how many incident waves and polarisation directions are needed and what level of mesh refinement is required to obtain the SSPs and phase matrix elements of the aggregate model in random orientation. In particular, we need to test if our findings from the comparisons between T-matrix methods for hexagonal columns carry over to more complex shapes such as the budding rosettes and rosette aggregates of our model. For the purposes of the database that will result from this paper, accuracy of a few percent is desired and ideally around 1%. This is to minimise costs from memory consumption, and total computational time, since the final simulations were carried out on AWS machines. Since no other (numerical or analytical) solutions exist for the aggregate model to compare with, we compare results between different mesh discretisations, number of incident waves and polarisation rotations.

We note that the goal here is not to provide a quantitative estimate of the accuracy of the boundary element method (accelerated or not), the preconditioned PM-CHWT formulation or the implementation in Bempp [75], but rather identify which parameter values to use for the database by balancing accuracy and computational cost.
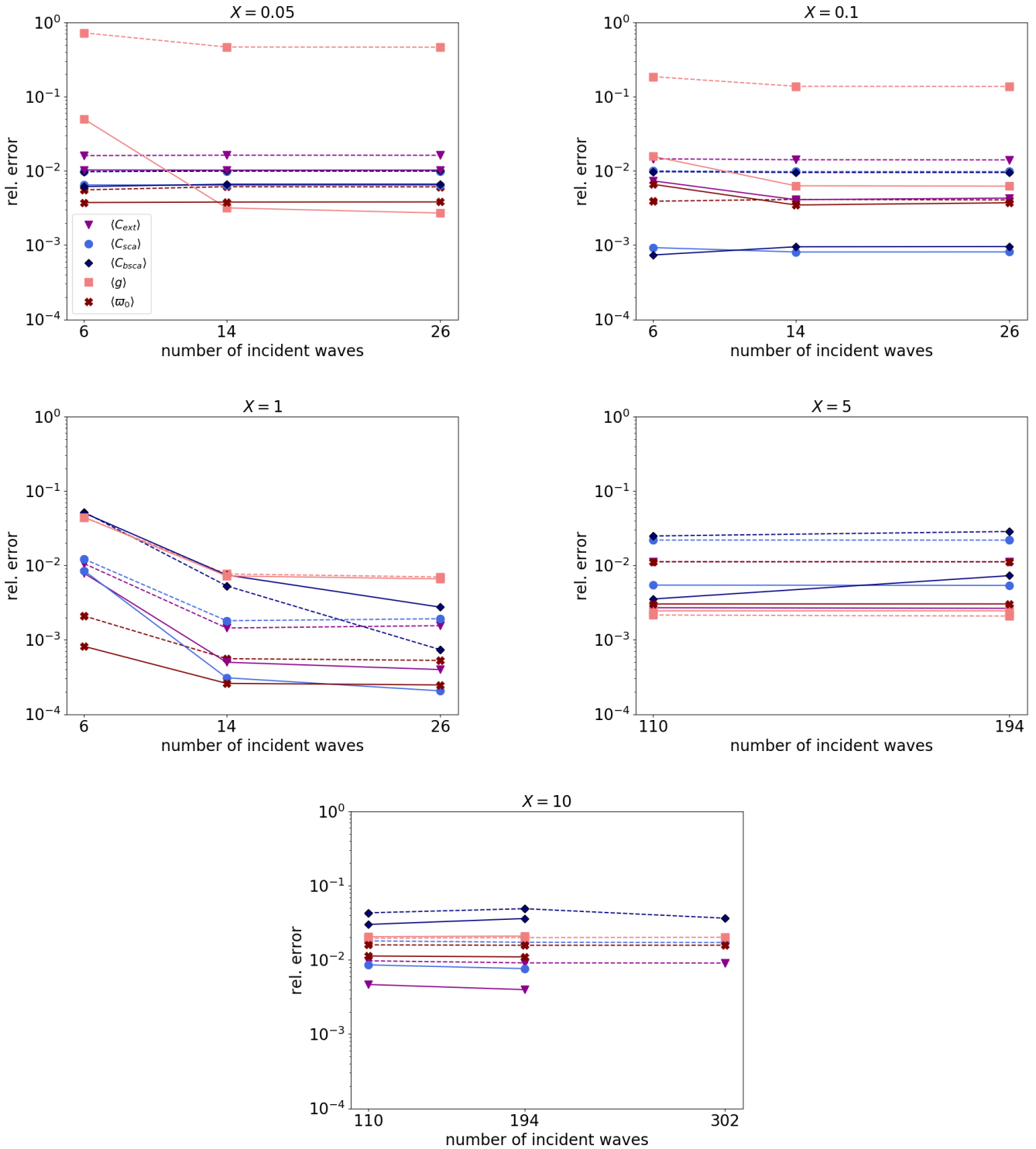
Figure 10: Relative errors of the SSPs as a function of increasing number of incoming waves for hexagonal columns of size parameter $X = 0.05$ (top left), $X = 0.1$ (top right), $X = 1$ (centre left), $X = 5$ (centre right) and $X = 10$ (bottom). A mesh size of 10 elements per wavelength was prescribed for the dashed lines resulting in a total of 36, 36, 180, 2968 and 6408 elements respectively. The solid lines represent refined meshes with 100 elements per wavelength for $X = 0.05$ and $X = 0.1$, and 20 elements per wavelength for $X = 1$, 5 and 10 resulting in a total of 60, 180, 612, 11652 and 14252 elements respectively.

17
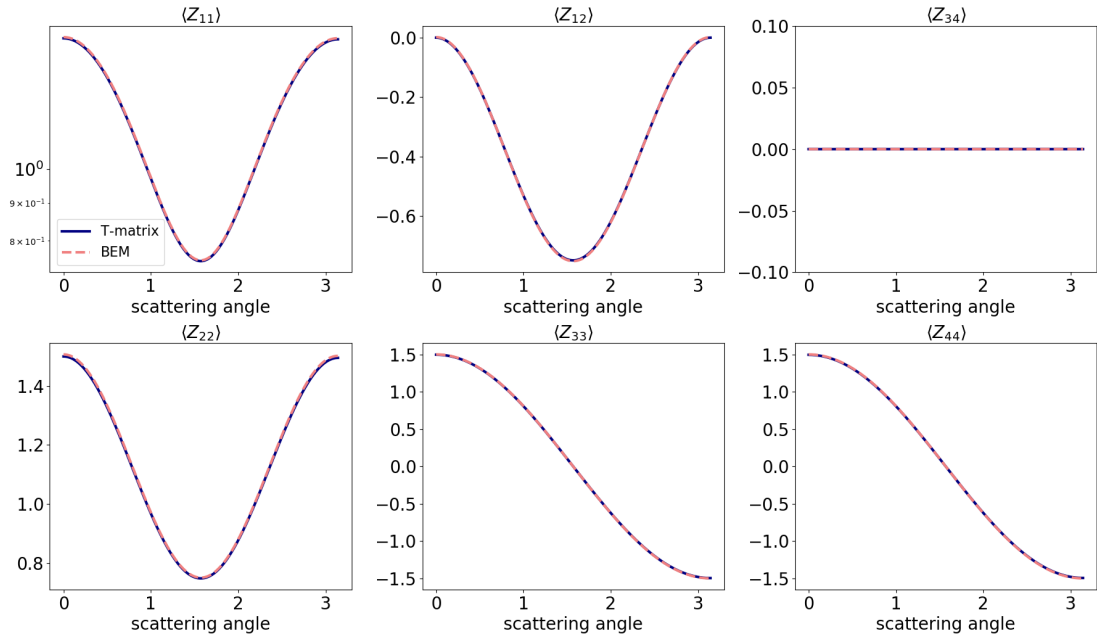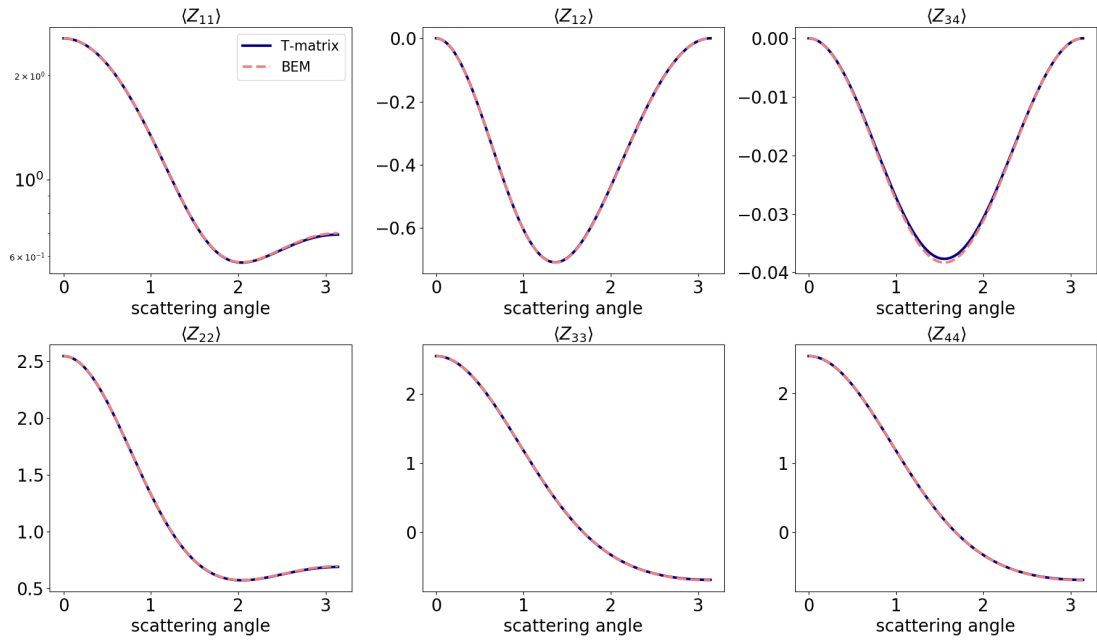
Figure 11: Phase matrix elements for hexagonal columns of size parameter (a) $X = 0.05$ and (b) $X = 1$. For (a) 14 incident waves and 5 polarisation rotations have been considered, while for (b) 14 incident waves and 10 polarisation rotations. We note that the remaining phase matrix elements are 0 when random orientation is assumed.
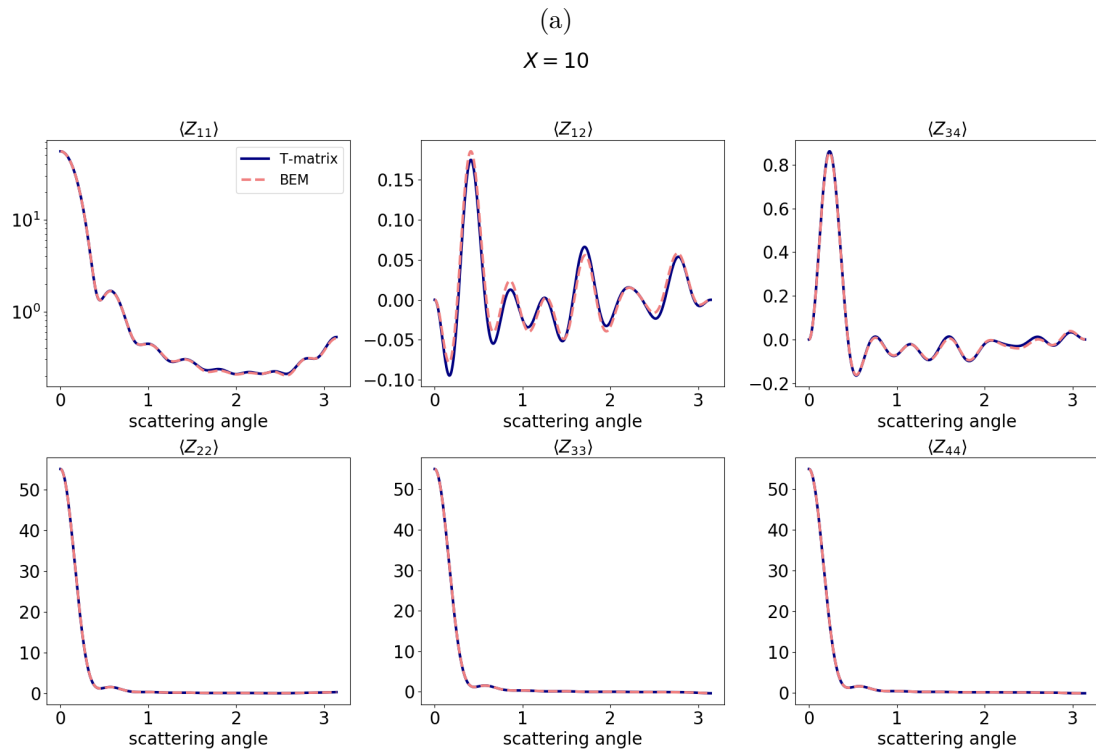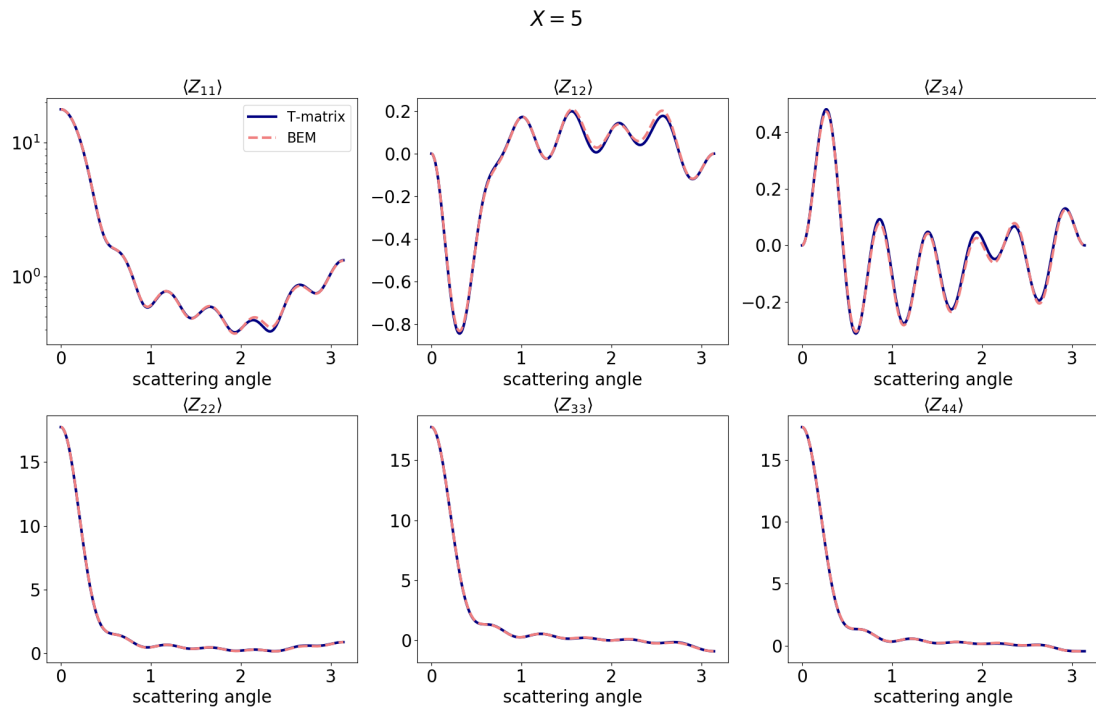
Figure 12: As in Figure 11 but for (a) $X = 5$ and (b) $X = 10$. In (a) 194 incident waves and 10 polarisations are considered and in (b) 194 incident waves and 15 polarisation rotations.

For further details regarding the method accuracy we refer to works such as [52] for earlier applications of BEM to ice crystals, [100] for discussions regarding the software framework for Bempp, [49] for initial work done on Calderón preconditioners, and [54, 82, 55] for accelerated BEM and its applications to scattering by complex aggregates. In what follows we compare results between different mesh discretisations, number of incident waves and polarisation rotations, by fixing all other parameters and only varying one at a time. Given that the real error depends on all three, it is likely that it is larger than what is shown here in each case. We also note that the real error and the difference between two mesh sizes (as considered in what follows) can be different and we refer the reader to sources cited earlier for more detailed discussions about mesh accuracy.

5.1. Mesh size

With regards to mesh refinement, we find that the usual rule of 10 elements per wavelength [52] is not a useful scheme as each aggregate consists of multiple smaller monomers, for which we need to achieve a sufficient discretisation for each surface. Taking a look at the aggregate model in Figures 4 - 7, we see our aggregates fall into 4 main categories, on which we also base our discretisation rules:

- $D_{max} = 10 - 492\mu m$: These are all re-scaled versions of $D_{max} = 492\mu m$ implying that the surfaces of each monomer shrink as D_{max} decreases. A minimum number of elements is imposed on such aggregates. After testing, these are: roughly 800 for 50 GHz, 4000 for 183 GHz, 8000 for 243 GHz and 13 000 for 664 GHz.

- $D_{max} = 547-875\mu m$, $1111-1190\mu m$, $1510-1630\mu m$: These are budding rosettes with very short branches. Each individual branch has a fixed size for all aggregates, so a constant number of elements per wavelength can be used. This is 100 elements per wavelength for 50 GHz, 80 for 183, 70 for 243 and 40 for 664 GHz.

- $D_{max} = 958 - 1045\mu m$, $1221 - 1461\mu m$, $1700 - 1759\mu m$, $2258\mu m$, $4115\mu m$, $4539\mu m$ and $5791\mu m$: These are budding rosettes with longer branches compared to the above category. As such a slightly relaxed mesh rule can be applied. Again, each monomer has a fixed size for all aggregates, so a constant number of elements per wavelength is used: 100 elements for 50 GHz, 50 for 183, 40 for 243 and 20 for 664 GHz.

- Remaining D_{max}: These are rosette aggregates, each rosette consists of 3 branches which are longer compared to the earlier categories. A relaxed mesh rule can be applied to those. We use 50 elements per wavelength at 50 GHz, 20 at 183, 20 at 243 and 10 or 20 at 664 GHz (we explain below).

Comparison between different mesh resolutions is performed for some test cases at all frequencies. In Tables 3 - 6 and Figure 13, we present some of those test cases at 664 GHz and -83°C, each table representing one of the above four categories. The results presented here are also found to be true at the other frequencies of 50, 183, and 243 GHz, and at the other temperatures, but are not presented for reasons of brevity.

We note that in Table 6, a relative difference of 1-2% is observed for some of the scattering cross-sections and a maximum relative difference of 5.1% for $\langle Z_{11} \rangle$ in Figure 13. The relative differences for the other phase matrix elements are not shown for reasons of brevity but they were as accurate. For aggregates $D_{max} > 4000\mu m$, at 664 GHz, the choice was made to run the simulations with a mesh size of 10 elements per wavelength despite the relative difference being more than 1%. This is because as D_{max} increases, so does the size parameter X and as seen in the following subsections, the number of incident waves and polarisation rotations need to increase with increasing X. Since the relative difference between the two mesh resolutions were below 5% (not shown for reasons of brevity) it was deemed acceptable to proceed with the mesh size of 10 elements per wavelength to reduce computational cost. The probability of occurrence of ice crystals with such large dimensions is also low, so a greater inaccuracy in the computation of SSPs is not going have as big an impact as the intermediate ones.

In addition, the SSPs and phase matrix elements of aggregates of size parameter $X = 0.2$ or smaller were computed using the Rayleigh approximation [101] for equivalent mass ice spheres, with the asymmetry parameter g computed from the T-matrix method of [102], otherwise the asymmetry parameter under the Rayleigh approximation would be zero. Contributions of such small size parameter ice crystals are very small to the volume integral SSPs over some ice crystal size spectrum so the choice was made to reduce computational time and cost and focus on the remaining size parameters that have a larger contribution in numerical weather and climate models.

5.2. Number of incident waves ($(\theta_i^{inc}, \phi_i^{inc})$ angles)

With regards to the number of incident waves required to achieve accuracy of a few percent for the SSPs, we find that these are dependent on the size parameter. For our aggregate model these are as follows:

X	# of incident waves	Order of Lebedev Scheme
$X < 1$	14	3
$1 \leq X < 3$	50	11
$3 \leq X < 5$	110	17
$5 \leq X < 8$	194	23
$8 \leq X < 10$	230	25
$X \geq 10$	302	29

D_{max}	$60\mu m$	$200\mu m$	$350\mu m$	$450\mu m$	$492\mu m$
$\langle C_{ext}\rangle$	0.02%	0.38%	0.05%	0.31%	0.37%
$\langle C_{sca}\rangle$	0.06%	0.08%	0.10%	0.11%	0.12%
$\langle C_{bsca}\rangle$	0.05%	0.06%	0.03%	0.13%	0.27%
$\langle g\rangle$	0.17%	0.05%	0.04%	0.01%	0.03%
$\langle \varpi_0\rangle$	0.10%	0.32%	0.07%	0.18%	0.46%
# of elements	8552 **13664**	8562 **13588**	8550 **13636**	8568 **13600**	8416 **13448**

Table 3: Relative difference between two different discretisation schemes for the smaller aggregates sizes $D_{max} \leq 492\mu m$ at 664 GHz, -83°C, with 14 incident waves. The bold font indicates the discretisation chosen for the SSPs, the non-bold refers to the alternative discretisation scheme considered. The relative differences are computed between the number of elements represented by the non-bold and bold fonts.

D_{max}	$547\mu m$	$697\mu m$	$1111\mu m$	$1190\mu m$	$1510\mu m$
$\langle C_{ext}\rangle$	0.60%	0.42%	0.22%	0.18%	0.25%
$\langle C_{sca}\rangle$	0.16%	0.10%	0.14%	0.18%	0.10%
$\langle C_{bsca}\rangle$	0.52%	0.66%	0.12%	0.09%	0.19%
$\langle g\rangle$	0.06%	0.06%	0.03%	0.09%	0.09%
$\langle \varpi_0\rangle$	0.43%	0.33%	0.34%	0.36%	0.35%
# of elements	6402 **12292**	9606 **15860**	19166 **31704**	25594 **42038**	28906 **47824**

Table 4: As in Table 3, but for two different discretisation schemes (30 and 40 elements per wavelength) for some of the short budding rosettes at 664 GHz, -83°C, with 194 incident waves. We note that relative differences between 20 and 30 elements per wavelength were all above 1% (and as high as 6% in some cases).

D_{max}	$958\mu m$	$1221\mu m$	$1700\mu m$	$2258\mu m$
$\langle C_{ext}\rangle$	0.05%	0.09%	0.11%	0.11%
$\langle C_{sca}\rangle$	0.25%	0.36%	0.37%	0.39%
$\langle C_{bsca}\rangle$	0.18%	0.40%	0.58%	0.16%
$\langle g\rangle$	0.04%	0.04%	0.05%	0.05%
$\langle \varpi_0\rangle$	0.20%	0.26%	0.26%	0.29%
# of elements	2064 **5464**	2920 **8186**	5814 **16248**	9326 **26332**

Table 5: As in Table 3, but for two different discretisation schemes (10 and 20 elements per wavelength) for some of the longer budding rosettes at 664 GHz,-83°C, with 194 incident waves.

D_{max}	$2121\mu m$	$3004\mu m$	$5508\mu m$	$6456\mu m$	$8582\mu m$
$\langle C_{ext}\rangle$	0.59%	0.75%	0.77%	0.78%	0.81%
$\langle C_{sca}\rangle$	<u>1.22%</u>	<u>1.29%</u>	<u>1.46%</u>	<u>1.50%</u>	<u>1.55%</u>
$\langle C_{bsca}\rangle$	0.70%	0.46%	0.65%	<u>1.14%</u>	<u>1.68%</u>
$\langle g\rangle$	0.11%	0.28%	0.17%	0.19%	0.19%
$\langle \varpi_0\rangle$	0.63%	0.54%	0.69%	0.72%	0.74%
# of elements	4404 **16516**	7040 **35368**	**29418** 110634	**39572** 147066	**43754** 162898
# of waves	194	230	230	230	230

Table 6: As in Table 3, but for two different discretisation schemes (10 and 20 elements per wavelength) for some of the aggregate rosettes at 664 GHz, -83°C. Red underlined values indicate that the relative difference is above 1% which is the desired accuracy.
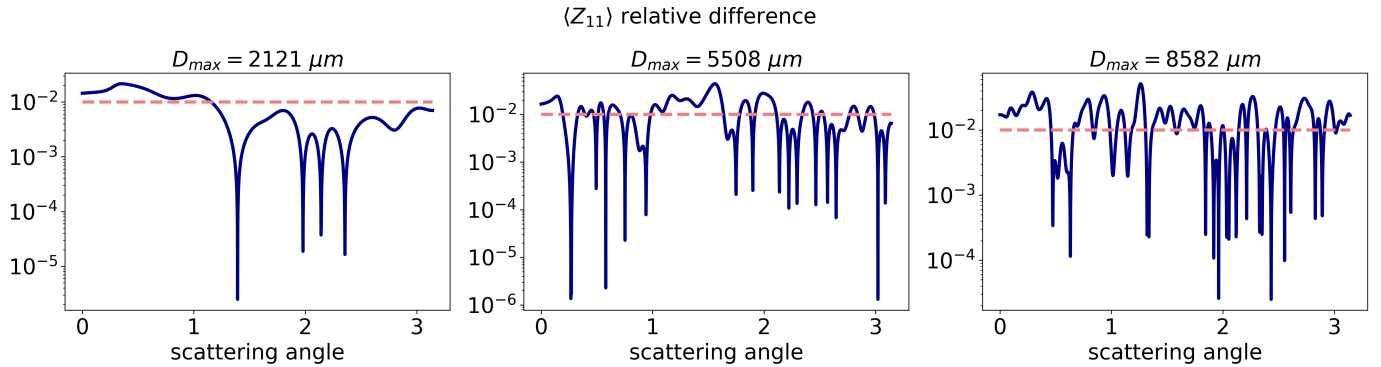
Figure 13: As in Table 6 but for $\langle Z_{11} \rangle$. The maximum relative difference observed is 2.2%, 4.4% and 5.1% respectively (left to right).

Numerical tests for some of the aggregates at 664 GHz can be seen in Tables 7 - 8 and Figures 14 - 17. We note that it is likely that as X increases beyond 10, the number of incident waves will also have to increase. However, for the purposes of the SSPs we limit the number to 302 to limit computational costs. Looking at the comparisons for the larger aggregates in Figures 14, 15 and 17 though, the relative difference still remains well under 10% when comparing results between 302 and 194 incident waves for $D_{max} = 5508\mu m$, while it reaches a maximum of 14.9% for $D_{max} = 8582\mu m$. Still, for the majority of the scattering angles the relative difference remains between 1 and 10%.

We also note that all SSPs except for C_{bsca} are approximated well at about 50 incident waves and it is the back-scattering cross-section that requires the additional incident waves. This is also evident in Figures 14 - 15 where a small error is observed (even between 14 and 302 incident waves) for all SSPs except the back-scattering cross-section. For future simulations, where the back-scattering cross-section is not of interest, computational costs can be reduced by reducing the number of incident waves.

In addition, we note that consistent with the comparisons of T-matrix results for hexagonal columns, no polarisation rotations (i.e. integration over γ) are required for the accurate computation of the integral optical properties, i.e., two incident polarisations are sufficient. This observation is also consistent with results from [61, 103, 104, 105, 98, 99].

5.3. Number of polarisation rotations (γ_i angles)

To evaluate the phase matrix elements of randomly oriented aggregates, in addition to the number of incident waves, we also need to consider the number of rotations of the polarisation directions. After testing, we find that those again depend on the size parameter as follows:

X	# of polarisation vectors
$X < 1$	10
$1 \leq X < 24$	15
$X \geq 24$	20

A selection of numerical experiments validating the above choice for some of the large model aggregates at 664 GHz and -83°C is shown in Figure 18. In Figure 18, we plot the relative difference of $\langle Z_{11} \rangle$ between 10 and 20 polarisation rotations (number of γ_i angles), for aggregates $D_{max} = 5508\mu m$ and $D_{max} = 8582\mu m$. We see that for the majority of the scattering angles the relative percentage difference lies between 1-10%, with some scattering angles reaching a relative percentage difference of roughly 30%.

Again, it is likely that more polarisation rotations will be needed as X grows but in combination with the number of incident waves the computational cost becomes increasingly high. For the largest aggregate sizes, 302×20 incident waves will have to be considered. These correspond to $2 \times 302 \times 20$ GMRES solves that need to be performed for each aggregate of $X \geq 24$, where the number of elements also increases with D_{max}. For the purposes of the SSPs we therefore limit the number of polarisation rotations to 20.

5.4. Comparing with other SSPs

5.4.1. Comparing simulation parameters

In the database by Guosheng Liu [61], the discrete dipole approximation (DDA) method [14, 106] was used to calculate the SSPs and phase matrix elements of ice columns and plates, rosettes and sector snowflakes of different maximum dimension and for different frequencies of incoming radiation. Two different causes were considered for the accuracy of the computed results: the interdipole spacing (similar to the mesh size of our method) and the number of orientations considered in simulating random orientation. An interdipole spacing scheme based on the wavelength (similar to a fixed number of elements per wavelength in our case) was considered. Comparison between the scheme used for the database and a scheme with half the spacing showed less than 2% relative errors for $\langle C_{sca} \rangle$ and $\langle g \rangle$ for all frequencies and particle sizes. The relative difference for $\langle C_{bsca} \rangle$ was higher but less than 5%. A total of $16 \times 17 \times 16 \ (= 4352)$ orientations were considered for the

D_{max}	$60\mu m$	$200\mu m$	$350\mu m$		$492\mu m$	
$\langle C_{ext} \rangle$	0.001%	0.009%	0.012%	0.000%	0.000%	0.000%
$\langle C_{sca} \rangle$	0.035%	0.009%	0.016%	0.000%	0.000%	0.000%
$\langle C_{bsca} \rangle$	0.039%	0.323%	9.448%	0.063%	2.442%	0.008%
$\langle g \rangle$	0.048%	0.006%	0.274%	0.000%	0.004%	0.000%
$\langle \varpi_0 \rangle$	0.068%	0.001%	0.007%	0.000%	0.000%	0.000%
# of waves	**14**	**14**	14	**50**	50	**110**
	50	50	50	110	110	194
X	0.41	1.31	2.43		3.42	
# of elements	13664	13588	13636		13448	

Table 7: Relative difference between different number of incident waves for the smaller aggregates sizes $D_{max} \leq 492\mu m$ at 664 GHz, -83°C. Red underlined values indicate that the relative difference is above 1% which is the desired accuracy. A relative difference of 0.000% indicates that the relative difference was below 0.001%. Bold font indicates the number of waves chosen for the database.

D_{max}	$547\mu m$	$697\mu m$	$805\mu m$	$1111\mu m$	$1190\mu m$	$1461\mu m$
$\langle C_{ext} \rangle$	0.000%	0.000%	0.000%	0.000%	0.000%	0.000%
$\langle C_{sca} \rangle$	0.000%	0.000%	0.000%	0.000%	0.000%	0.000%
$\langle C_{bsca} \rangle$	0.001%	0.249%	1.263%	0.198%	1.217%	2.618%
$\langle g \rangle$	0.000%	0.000%	0.001%	0.000%	0.09%	0.001%
$\langle \varpi_0 \rangle$	0.000%	0.000%	0.000%	0.000%	0.36%	0.000%
# of waves	**110**	**110**	110	**194**	194	230
	194	194	**194**	230	**230**	**302**
X	3.80	4.84	5.59	7.73	8.28	10.2
# of elements	12292	15860	16022	31704	42038	11280

Table 8: As in Table 7 but for some of the short budding rosettes at 664 GHz, -83°C.
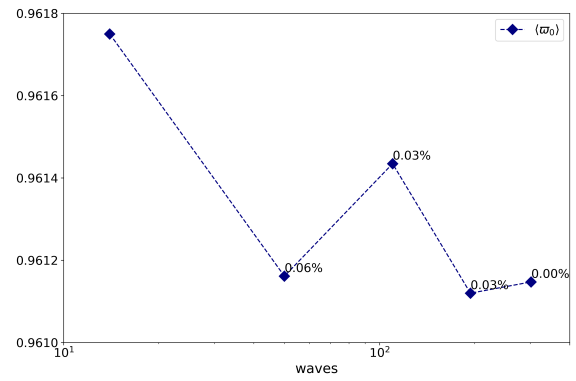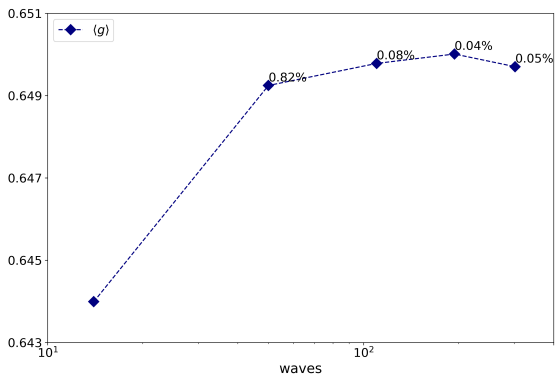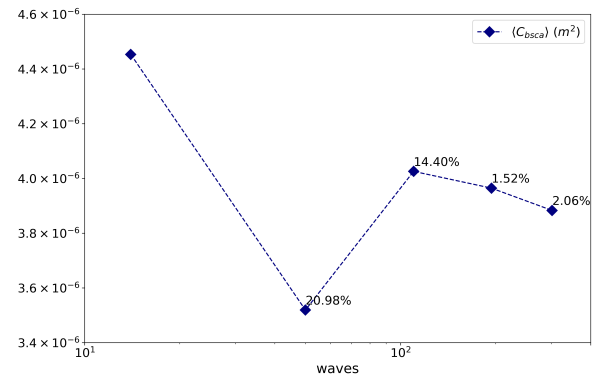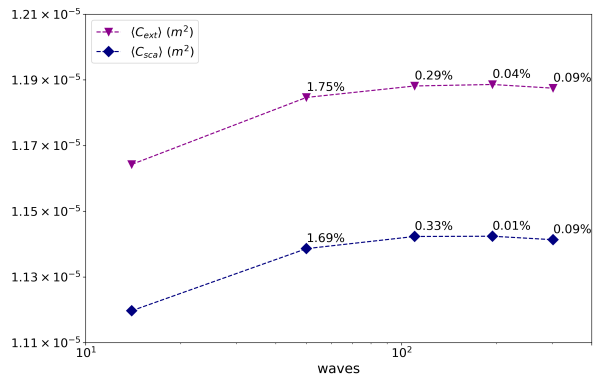
Figure 14: SSPs as a function of increasing number of incoming waves (14, 50, 110, 194, 302) for the aggregate $D_{max} = 5508\mu m$ at 664 GHz, -83°C. Relative difference percentage is shown between the current and previous number of incident waves. The size parameter is $X = 38.3$ and the number of elements used for the discretisation is 29418. As a reference, the relative difference percentages between 302 (max) and 14 (min) incident waves are 1.99%, 1.93%, 12.80%, 0.89% and 0.06% for $\langle C_{ext} \rangle$, $\langle C_{sca} \rangle$, $\langle C_{bsca} \rangle$, $\langle g \rangle$ and $\langle \varpi_0 \rangle$ respectively.
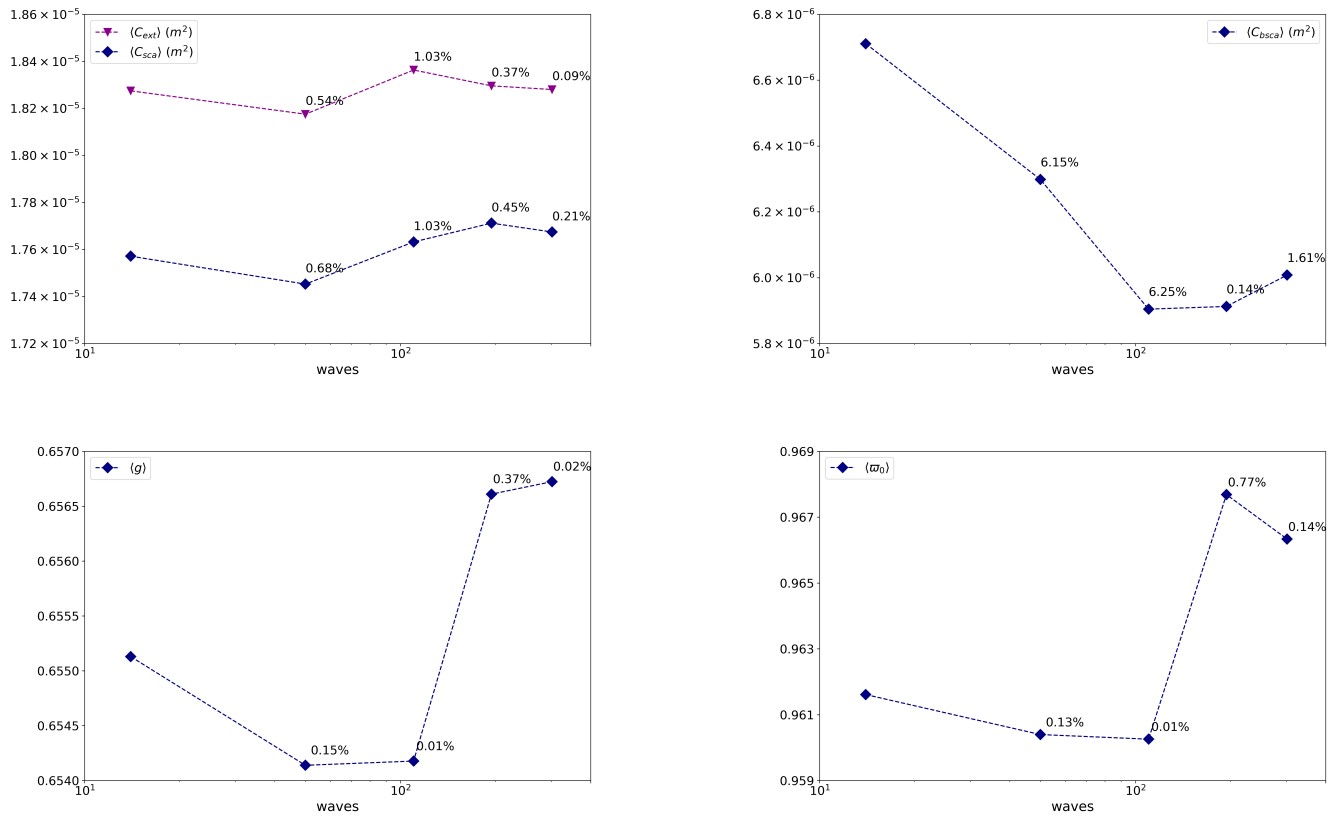
Figure 15: As in Figure 14 but for $D_{max} = 8582\mu m$. The size parameter is $X = 59.7$ and the number of elements used for the discretization is 43754. The relative difference percentages between 302 (max) and 14 (min) incident waves are 0.03%, 0.59%, 10.48%, 0.24% and 0.49% for $\langle C_{ext} \rangle$, $\langle C_{sca} \rangle$, $\langle C_{bsca} \rangle$, $\langle g \rangle$ and $\langle \varpi_0 \rangle$ respectively.
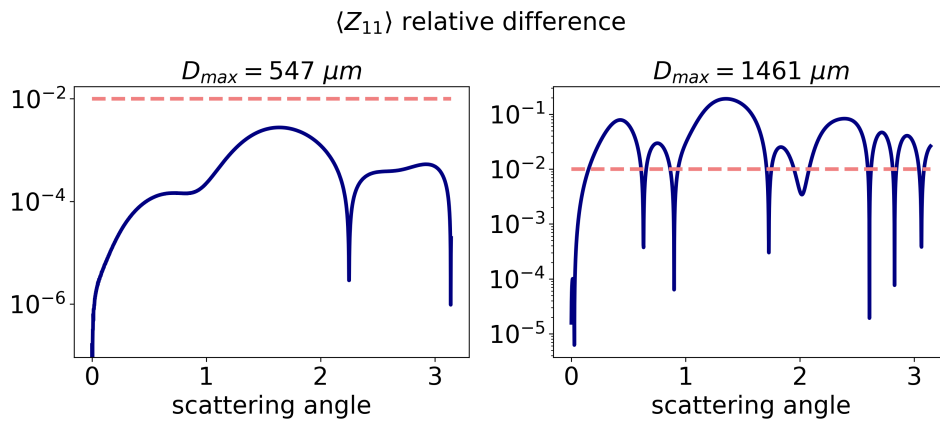

Figure 16: As in Table 8 but for $\langle Z_{11} \rangle$. The maximum relative difference observed is 0.2% and 19.1% respectively (left to right). The dashed line indicates a 1% relative difference.
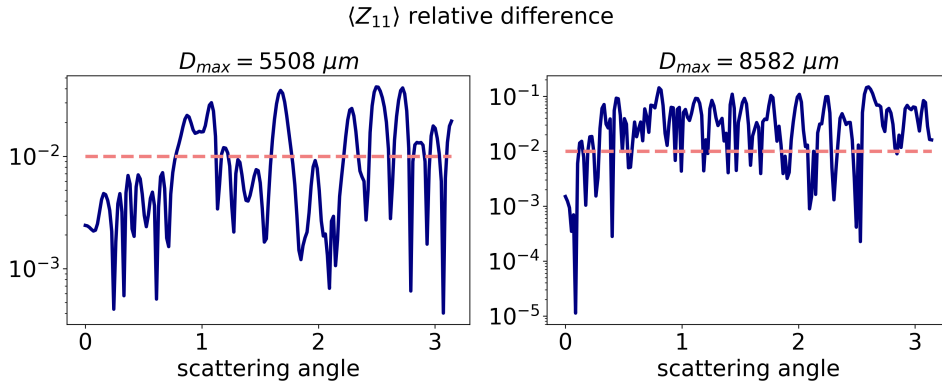
Figure 17: Relative difference for $\langle Z_{11} \rangle$ between 194 and 302 incident incoming waves for $D_{max} = 5508\mu m$ and $8582~\mu m$. Other parameters are as in Figures 14 and 15. The maximum relative difference observed is 4.15% and 14.9% (left to right).

Figure 18: Relative difference for $\langle Z_{11} \rangle$ between 10 and 20 polarisation rotations (γ_i angles) for $D_{max} = 5508\mu m$ and $8582~\mu m$. Other parameters are as in Figures 14 and 15. The maximum relative difference observed is 29.6% and 28.9% (left to right). The dashed lines represent a 1%, 10% and 20% relative difference.
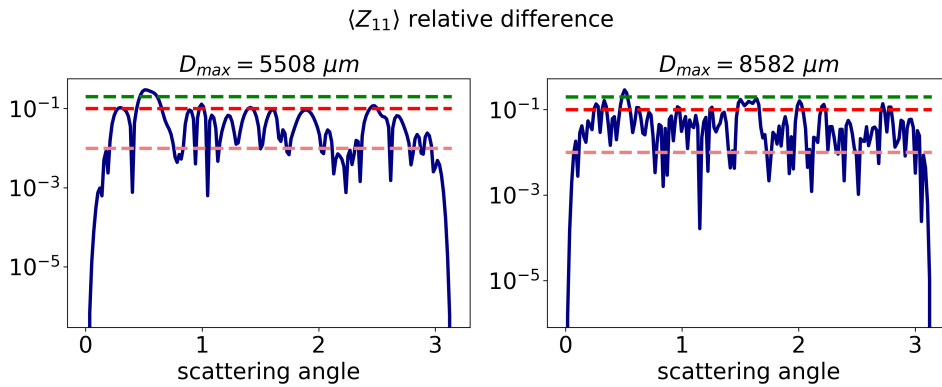
simulations of the database. To test whether this number of orientations was 'random' enough tests were also performed with $32 \times 33 \times 32$ (= 33792) orientations. The relative difference for $\langle C_{sca} \rangle$ and $\langle g \rangle$ was less than 1%, however the relative difference for $\langle C_{bsca} \rangle$ increased with frequency and particle size. While for lower frequencies the relative difference was less than 5% this increased to more than 20% for higher frequencies and larger particles.

These observations are consistent with ours, i.e. the number of incident waves required to accurately compute $\langle C_{bsca} \rangle$ increases with X, while the remaining scattering properties are accurately computed with a smaller number of them, about 50 incident waves in our case. As mentioned earlier, this is also consistent with results from [103, 104, 105, 98, 99].

We note though that in DDA simulations, computations for γ are cheap, and might not necessarily have been optimised compared to the other two - meaning that more computations have been performed than required [99]. Given that no discussion is given in [61] regarding this optimisation, a fair comparison of the total number of orientations might not be possible.

Finally, we note that Lebedev quadrature outperforms the quadratures used in packages such as DDSCAT [106] or ADDA [107], but could be easily employed with the DDA methods. It is not specific to the boundary element method, but rather specific to this implementation presented here. In fact, it has already been employed by others such as in the work by Fenni *et al.* [98]. In general, fair comparisons between different software or different approximation methods are not always feasible as implementations are usually optimized for the hardware and architecture available to those developing and using the methods. Still, relevant to this paper, Yurkin [99] has formulated guidelines for a fair evaluation of orientation-averaging methods for light-scattering simulations and we refer the reader there for further details.

5.4.2. Comparing simulation results

In Figures 19 - 20 we compare the optical properties of the rosette aggregates used here at 243 GHz, -83°C with those of the compact eight-branched hexagonal ice aggregate [64], the six-branched bullet rosette [64] and the ARTS large column aggregate models [64]. The reason as to why these models were chosen is because the latter two are the better performing models in the study by Fox [2], when compared with the observations, whereas the compact eight-branched hexagonal aggregate model is the worst performing model out of all other models. In those figures, the rosette aggregate model simulations of these integral optical properties follow the two best performing models as a function of frequency rather nicely in the D^2_{max} regime. The cross sections of the compact eight-branched hexagonal ice aggregate generally diverge significantly from the others in the D^2_{max} regime, because it is too compact and has too much mass, which is why it performs so poorly when compared with the observations.

5.5. Notes on implementation

For the simulation of the scattering properties for this database the open source library Bempp [75] (Versions 3.3.4 and 3.3.5) has been used with the accelerating methods of [54, 55]. Amazon Web Services (AWS) EC2 instances were used to perform our simulations with up to 96 CPUs available at a time and 384 GB of RAM. Smaller size parameter problems were ran on a desktop machine with 40 CPUs and 188 GB RAM. Given the large availability of CPUs, the Multiprocessing library in Python was used to distribute the different incoming waves and therefore run multiple GMRES solves in parallel aiming to reduce total computation time.

6. Discussion

In this paper, it has been demonstrated for the first time that BEM can be applied to solve for the light scattering properties of very complex ice particles that occur in the Earth's atmosphere. To the best of our knowledge, this level of particle complexity over such a size parameter range has not been investigated or previously presented using BEM applied to realistic atmospheric ice crystals. Here, we have developed a model of budding rosettes and rosette aggregates that is based on observations of the most commonly occurring habits found within in-situ generated cirrus, and these habits contributed mostly to the total mass, and the orientation-averaged projected area frequency of occurrence statistics found within that cloud type. The budding rosette and rosette aggregate models were generated using a Monte-Carlo model that includes realistic fall speeds of ice crystals, generating 65 models between the maximum dimensions of between 10 and 10,000μm. However, the mass of the rosette aggregates were constructed to follow an observed mass-dimension relation that is assumed within the cloud microphysics scheme of the Met Office's operational global Unified Model. This was done to ensure physical consistency between the weather and climate model assumptions in their microphysics schemes, and the single-scattering properties. This being important because the single-scattering properties will be utilised to simulate forthcoming observations from space-based microwave and sub-millimetre instruments using the weather model's predictions of ice mass. Of course, these same single-scattering properties may also be applied to the inverse problem in retrieving cloud ice macrophysical and microphysical properties from those instruments. We have shown that the Monte Carlo generated rosette aggregate models are generally within ±30% of the chosen mass-dimension relation. Moreover, we have further demonstrated that the observed area-dimension relation found for in-situ generated cirrus are within the standard deviation of the orientation-averaged projected areas of the rosette aggregate models. Therefore, these models using BEM can also be applied to generate single-scattering properties across the electromagnetic spectrum other than at microwave frequencies.
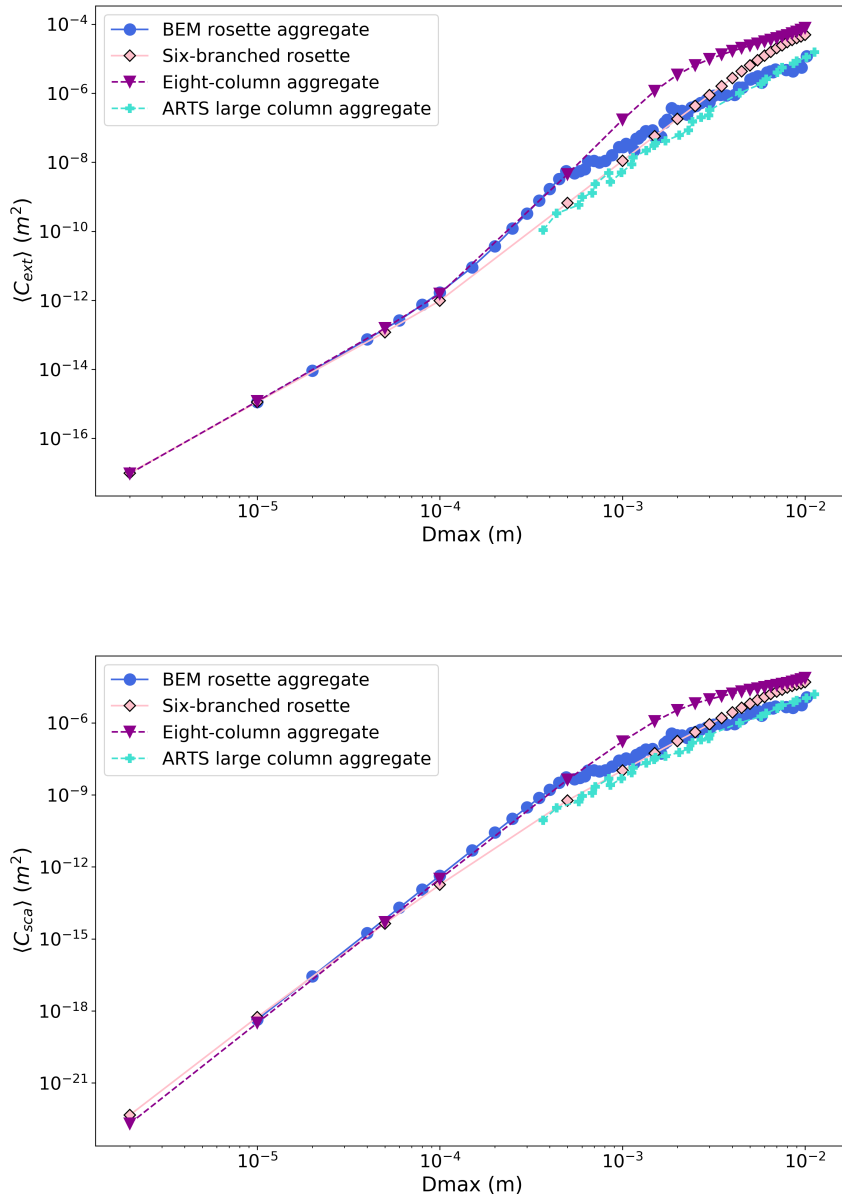
Figure 19: Scattering properties $\langle C_{ext} \rangle$ (top) and $\langle C_{sca} \rangle$ (bottom) of the rosette aggregates of Figures 4 - 7, the compact eight-branched hexagonal ice aggregate [64], the six-branched bullet rosette [64] and the ARTS large column aggregate models [64].

This paper concentrates on BEM optimal settings that are applicable to microwave and sub-millimetre scattering at the frequencies of 50, 183, 243, and 664 GHz for the temperature values of -83°C, -43°C, and -3°C. This is because there is a need to generate single-scattering properties of realistic ice crystals that are consistent with weather model ice microphysics assumptions at those frequencies to take advantage of forthcoming weather satellites for the purposes of assimilation of all-sky radiance measurements into the Met Office's UM. However, the scattering properties developed here are not only applicable to the Met Office's UM but also to other weather and climate centres as well, owing to the mass-dimension relation on which they are based being generally applicable to cold ice cloud. The size parameter range over which the BEM generated single-scattering properties are calculated in this paper is between 0.29 and approximately 72. However, the higher size parameter at 664 GHz does not represent the upper limit of BEM but rather the cost of utilising the AWS resources at the time. In the near future there will be no such limitations.

The computation of the single-scattering properties assumes random orientation because this is a necessary condition for efficiently solving the equation of radiative trans-
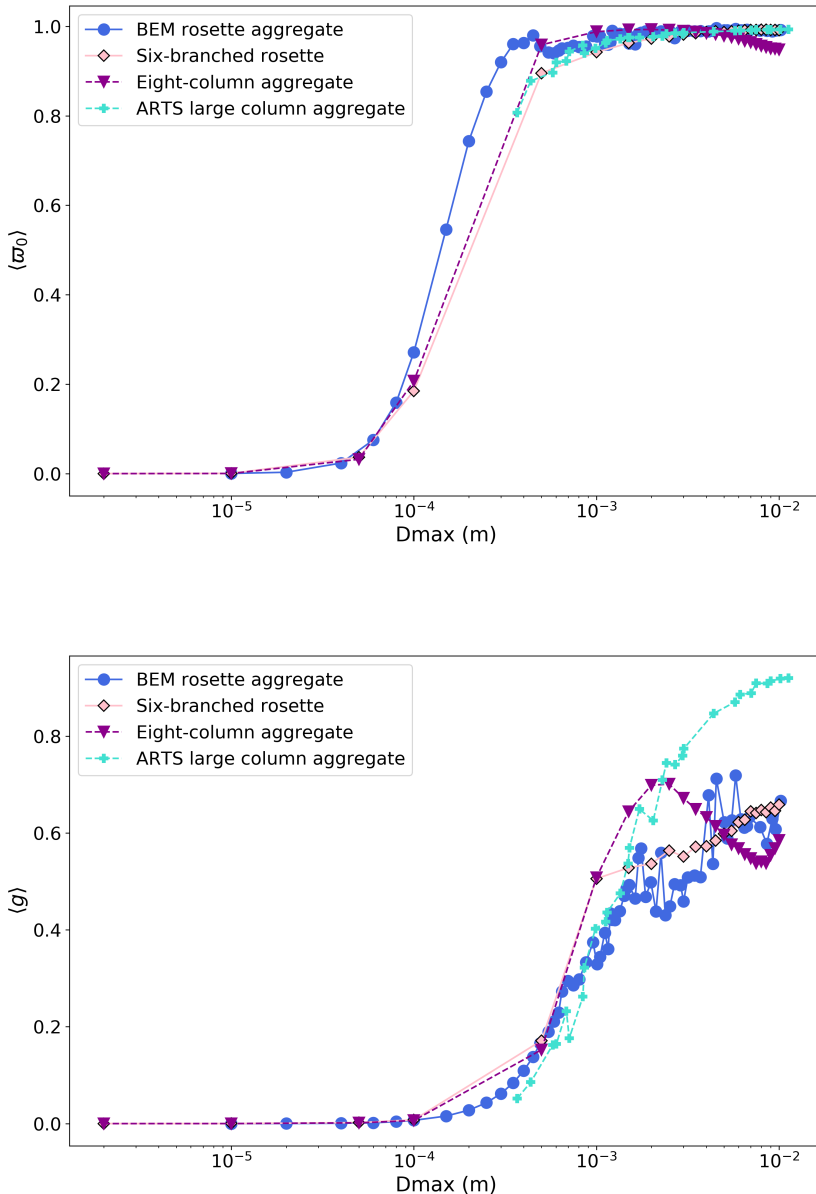
Figure 20: As in Figure 19 but for $\langle \varpi_0 \rangle$ (top) and $\langle g \rangle$ (bottom).

fer in weather and climate models. To represent random orientation, we take advantage of the BEM generated linear matrix equation, which is more effectively solved for by fixing the particle with respect to the incident plane wave and allowing the incident wave to rotate about the particle. This approach to random orientation is different to the more traditional set ups which fix the incident direction of the plane wave and rotate the particle instead with respect to that incident wave. We have demonstrated the accuracy of this interpretation by replicating T-matrix single-scattering property solutions found for hexagonal columns to within a few percent for size parameters between 0.05 and 10. In respect to the mesh size, we find

that the usual BEM rule of 10 elements per wavelength is not a general condition because it is found to be dependent on the size parameter. After careful analysis, the number of elements per wavelength that should be applied to solve for the single-scattering properties of the budding rosettes, and rosette aggregates has been carefully tabulated in this paper. Generally, it is found that if the appropriate number of elements per wavelength is applied, the errors in calculating the integral optical properties can be reduced to generally less than 2% without increasing the memory or solution times to onerous values. Likewise, the number of incident waves required for accurate calculation of the single-scattering properties also depends on the size

parameter. Generally, we find that 14 and up to 302 incident waves for the smallest and largest size parameters of up to about 70, respectively, can be assumed to minimise the single-scattering property errors found for the total optical properties to be generally less than a few percent, with the errors growing larger (in the area of 15%) for some of the largest size parameters considered here. Further, we find that again, to minimise the single-scattering property errors, the number of polarisation "directions" is also size parameter dependent. The number required between the size parameters of less than one and greater than or equal to 24 is between 10, and 20, respectively.

We conclude that the BEM is a method which can be applied to very complex realistic ice aggregates that occur in the Earth's atmosphere to compute their single-scattering properties to within an accuracy of most generally less than a few percent if the correct parameter settings are applied. This is sufficiently accurate to apply to weather and climate models, as well as to the remote-sensing of cirrus and ice cloud properties. The single-scattering properties are currently in production. The properties for 50, 183 and 243 GHz are currently available[1], the database will be updated with those for 664 GHz once they are available. This is expected to be by the end of 2023.

CRediT authorship contribution statement

Antigoni Kleanthous: Conceptualization, methodology, software, validation, formal analysis, writing–original draft preparation, writing–review and editing, visualization. **Anthony J. Baran:** Conceptualization, methodology, validation, formal analysis, resources, writing–original draft preparation, writing–review and editing, visualization, supervision, project administration, funding acquisition. **Timo Betcke:** Methodology, software, resources, writing–review and editing, supervision, funding acquisition. **David P. Hewett:** Methodology, writing–review and editing, supervision. **Christopher D. Westbrook:** Methodology, writing–review and editing.

Declaration of competing interest

The authors declare that they have no known competing financial interests or personal relationships that could have appeared to influence the work reported in this paper.

Acknowledgements

---

[1] https://zenodo.org/deposit/7962330

References

[1] A. J. Geer, K. Lonitz, P. Weston, M. Kazumori, K. Okamoto, Y. Zhu, E. H. Liu, A. Collard, W. Bell, S. Migliorini, et al., All-sky satellite data assimilation at operational weather forecasting centres, Quarterly Journal of the Royal Meteorological Society 144 (713) (2018) 1191–1217.

[2] S. Fox, An Evaluation of Radiative Transfer Simulations of Cloudy Scenes from a Numerical Weather Prediction Model at Sub-Millimetre Frequencies Using Airborne Observations, Remote Sensing 12 (17) (2020) 2758.

[3] V. Kangas, S. D'Addio, U. Klein, M. Loiselet, G. Mason, J.-C. Orlhac, R. Gonzalez, M. Bergada, M. Brandt, B. Thomas, Ice cloud imager instrument for MetOp Second Generation, in: 2014 13th Specialist Meeting on Microwave Radiometry and Remote Sensing of the Environment (MicroRad), IEEE, 2014, pp. 228–231.

[4] K. F. Evans, S. J. Walter, A. J. Heymsfield, M. N. Deeter, Modeling of submillimeter passive remote sensing of cirrus clouds, Journal of Applied Meteorology and Climatology 37 (2) (1998) 184–205.

[5] S. A. Buehler, C. Jiménez, K. F. Evans, P. Eriksson, B. Rydberg, A. J. Heymsfield, C. J. Stubenrauch, U. Lohmann, C. Emde, V. O. John, et al., A concept for a satellite mission to measure cloud ice water path, ice particle size, and cloud altitude, Quarterly Journal of the Royal Meteorological Society: A journal of the atmospheric sciences, applied meteorology and physical oceanography 133 (S2) (2007) 109–128.

[6] P. Eriksson, M. Jamali, J. Mendrok, S. A. Buehler, On the microwave optical properties of randomly oriented ice hydrometeors, Atmospheric Measurement Techniques 8 (5) (2015) 1913–1933.

[7] A. J. Baran, H. Ishimoto, O. Sourdeval, E. Hesse, C. Harlow, The applicability of physical optics in the millimetre and sub-millimetre spectral region. Part II: Application to a three-component model of ice cloud and its evaluation against the bulk single-scattering properties of various other aggregate models, Journal of Quantitative Spectroscopy and Radiative Transfer 206 (2018) 83–100.

[8] S. Fox, J. Mendrok, P. Eriksson, R. Ekelund, S. J. O'Shea, K. N. Bower, A. J. Baran, R. C. Harlow, J. C. Pickering, Airborne validation of radiative transfer modelling of ice clouds at millimetre and sub-millimetre wavelengths, Atmospheric Measurement Techniques 12 (3) (2019) 1599–1617.

[9] A. J. Baran, A review of the light scattering properties of cirrus, Journal of Quantitative Spectroscopy and Radiative Transfer 110 (14) (2009) 1239–1260.

[10] A. J. Baran, From the single-scattering properties of ice crystals to climate prediction: A way forward, Atmospheric Research 112 (2012) 45–69.

[11] P. Yang, K.-N. Liou, L. Bi, C. Liu, B. Yi, B. A. Baum, On the radiative properties of ice clouds: Light scattering, remote sensing, and radiation parameterization, Advances in Atmospheric Sciences 32 (1) (2015) 32–63.

[12] R. Lawson, S. Woods, E. Jensen, E. Erfani, C. Gurganus, M. Gallagher, P. Connolly, J. Whiteway, A. Baran, P. May, et al., A review of ice particle shapes in cirrus formed in situ and in anvils, Journal of Geophysical Research: Atmospheres 124 (17-18) (2019) 10049–10090.

[13] M. I. Mishchenko, Electromagnetic scattering by particles and particle groups: an introduction, Cambridge University Press, 2014.

[14] B. T. Draine, P. J. Flatau, Discrete-dipole approximation for scattering calculations, JOSA A 11 (4) (1994) 1491–1499.

[15] M. A. Yurkin, A. G. Hoekstra, The discrete dipole approximation: an overview and recent developments, Journal of Quantitative Spectroscopy and Radiative Transfer 106 (1-3) (2007) 558–589.

[16] P. Yang, K. Liou, Finite-difference time domain method for light scattering by small ice crystals in three-dimensional space, JOSA A 13 (10) (1996) 2072–2085.

[17] P. Yang, K. Liou, Finite difference time domain method for light scattering by nonspherical and inhomogeneous particles, in: Light Scattering by Nonspherical Particles: Theory, Measurements, and Applications, Vol. 1, Academic, 2000, p. 174.

[18] M. A. Yurkin, A. G. Hoekstra, R. S. Brock, J. Q. Lu, Systematic comparison of the discrete dipole approximation and the finite difference time domain method for large dielectric scatterers, Optics Express 15 (26) (2007) 17902–17911.

[19] C. Liu, L. Bi, R. L. Panetta, P. Yang, M. A. Yurkin, Comparison between the pseudo-spectral time domain method and the discrete dipole approximation for light scattering simulations, Optics Express 20 (15) (2012) 16763–16776.

[20] S. Havemann, A. Baran, Extension of T-matrix to scattering of electromagnetic plane waves by non-axisymmetric dielectric particles: application to hexagonal ice cylinders, Journal of Quantitative Spectroscopy and Radiative Transfer 70 (2) (2001) 139–158.

[21] A. J. Baran, P. Yang, S. Havemann, Calculation of the single-scattering properties of randomly oriented hexagonal ice columns: a comparison of the T-matrix and the finite-difference time-domain methods, Applied optics 40 (24) (2001) 4376–4386.

[22] M. Kahnert, The T-matrix code Tsym for homogeneous dielectric particles with finite symmetries, Journal of Quantitative Spectroscopy and Radiative Transfer 123 (2013) 62–78.

[23] L. Bi, P. Yang, G. W. Kattawar, M. I. Mishchenko, Efficient implementation of the invariant imbedding T-matrix method and the separation of variables method applied to large non-spherical inhomogeneous particles, Journal of Quantitative Spectroscopy and Radiative Transfer 116 (2013) 169–183.

[24] L. Bi, P. Yang, Accurate simulation of the optical properties of atmospheric ice crystals with the invariant imbedding T-matrix method, Journal of Quantitative Spectroscopy and Radiative Transfer 138 (2014) 17–35.

[25] K. Muinonen, Scattering of light by crystals: a modified Kirchhoff approximation, Applied optics 28 (15) (1989) 3044–3050.

[26] K. Muinonen, T. Nousiainen, P. Fast, K. Lumme, J. Peltoniemi, Light scattering by Gaussian random particles: ray optics approximation, Journal of Quantitative Spectroscopy and Radiative Transfer 55 (5) (1996) 577–601.

[27] A. Macke, J. Mueller, E. Raschke, Single scattering properties of atmospheric ice crystals, Journal of the Atmospheric Sciences 53 (19) (1996) 2813–2825.

[28] P. Yang, K. Liou, Geometric-optics–integral-equation method for light scattering by nonspherical ice crystals, Applied optics 35 (33) (1996) 6568–6584.

[29] M. I. Mishchenko, A. Macke, Incorporation of physical optics effects and computation of the Legendre expansion for ray-tracing phase functions involving δ-function transmission, Journal of Geophysical Research: Atmospheres 103 (D2) (1998) 1799–1805.

[30] K.-N. Liou, An introduction to atmospheric radiation, Elsevier, 2002.

[31] A. G. Borovoi, I. A. Grishin, Scattering matrices for large ice crystal particles, JOSA A 20 (11) (2003) 2071–2080.

[32] E. Hesse, Modelling diffraction during ray tracing using the concept of energy flow lines, Journal of Quantitative Spectroscopy and Radiative Transfer 109 (8) (2008) 1374–1383.

[33] L. Bi, P. Yang, G. W. Kattawar, B. A. Baum, Y. X. Hu, D. M. Winker, R. S. Brock, J. Q. Lu, Simulation of the color ratio associated with the backscattering of radiation by ice particles at the wavelengths of 0.532 and 1.064 μm, Journal of Geophysical Research: Atmospheres 114 (D4) (2009).

[34] L. Bi, P. Yang, G. W. Kattawar, Y. Hu, B. A. Baum, Scattering and absorption of light by ice particles: solution by a new physical-geometric optics hybrid method, Journal of Quantitative Spectroscopy and Radiative Transfer 112 (9) (2011) 1492–1508.

[35] E. Hesse, A. Macke, S. Havemann, A. Baran, Z. Ulanowski, P. H. Kaye, Modelling diffraction by facetted particles, Journal of Quantitative Spectroscopy and Radiative Transfer 113 (5)

(2012) 342–347.

[36] L. Bi, P. Yang, C. Liu, B. Yi, B. A. Baum, B. Van Diedenhoven, H. Iwabuchi, Assessment of the accuracy of the conventional ray-tracing technique: Implications in remote sensing and radiative transfer involving ice clouds, Journal of Quantitative Spectroscopy and Radiative Transfer 146 (2014) 158–174.

[37] W. Hackbusch, Hierarchical matrices: algorithms and analysis, Vol. 49, Springer, 2015.

[38] M. Bebendorf, Hierarchical matrices, Springer, 2008.

[39] S. Börm, Efficient numerical methods for non-local operators: H2-matrix compression, algorithms and analysis, Vol. 14, European Mathematical Society, 2010.

[40] S. Omar, D. Jiao, O (N) iterative and O (NlogN) direct volume integral equation solvers for large-scale electrodynamic analysis, in: 2014 International Conference on Electromagnetics in Advanced Applications (ICEAA), IEEE, 2014, pp. 593–596.

[41] B. Dembart, E. Yip, The accuracy of fast multipole methods for Maxwell's equations, IEEE Computational Science and Engineering 5 (3) (1998) 48–56.

[42] E. Darve, The fast multipole method: numerical implementation, Journal of Computational Physics 160 (1) (2000) 195–240.

[43] N. A. Gumerov, R. Duraiswami, Fast multipole method for the biharmonic equation in three dimensions, Journal of Computational Physics 215 (1) (2006) 363–383.

[44] A. J. Poggio, E. K. Miller, Integral equation solutions of three-dimensional scattering problems, MB Assoc., 1970.

[45] T.-K. Wu, L. L. Tsai, Scattering from arbitrarily-shaped lossy dielectric bodies of revolution, Radio Science 12 (5) (1977) 709–718.

[46] J. R. Mautz, R. F. Harrington, Electromagnetic scattering from a homogeneous body of revolution, Tech. rep., Syracuse Univ. NY Dept. of Electrical and Computer Engineering (1977).

[47] R. F. Harrington, Boundary integral formulations for homogeneous material bodies, Journal of electromagnetic waves and applications 3 (1) (1989) 1–15.

[48] S. Yan, J.-M. Jin, Z. Nie, A comparative study of Calderón preconditioners for PMCHWT equations, IEEE transactions on Antennas and Propagation 58 (7) (2010) 2375–2383.

[49] K. Cools, F. P. Andriulli, E. Michielssen, A Calderón multiplicative preconditioner for the PMCHWT integral equation, IEEE transactions on Antennas and Propagation 59 (12) (2011) 4579–4587.

[50] K. Niino, N. Nishimura, Calderón preconditioning approaches for PMCHWT formulations for Maxwell's equations, International Journal of Numerical Modelling: Electronic Networks, Devices and Fields 25 (5-6) (2012) 558–572.

[51] P. Ylä-Oijala, S. P. Kiminki, Challenges in developing efficient Calderón preconditioners for resonating or high material contrast penetrable objects, Journal of Computational and Applied Mathematics 289 (2015) 296–305.

[52] S. P. Groth, A. J. Baran, T. Betcke, S. Havemann, W. Śmigaj, The boundary element method for light scattering by ice crystals and its implementation in BEM++, Journal of Quantitative Spectroscopy and Radiative Transfer 167 (2015) 40–52.

[53] A. J. Baran, S. P. Groth, The application of the boundary element method in BEM++ to small extreme Chebyshev ice particles and the remote detection of the ice crystal number concentration of small atmospheric ice particles, Journal of Quantitative Spectroscopy and Radiative Transfer 198 (2017) 68–80.

[54] A. Kleanthous, T. Betcke, D. P. Hewett, M. W. Scroggs, A. J. Baran, Calderón preconditioning of PMCHWT boundary integral equations for scattering by multiple absorbing dielectric particles, Journal of Quantitative Spectroscopy and Radiative Transfer 224 (2019) 383–395.

[55] A. Kleanthous, T. Betcke, D. P. Hewett, P. Escapil-Inchauspé, C. Jerez-Hanckes, A. J. Baran, Accelerated Calderón preconditioning for Maxwell transmission problems, Journal of Com-

putational Physics (2022) 111099.

[56] R. Hiptmair, Operator preconditioning, Computers and mathematics with Applications 52 (5) (2006) 699–706.

[57] A. Buffa, S. Christiansen, A dual finite element complex on the barycentric refinement, Mathematics of Computation 76 (260) (2007) 1743–1769.

[58] Y. Mano, Exact solution of electromagnetic scattering by a three-dimensional hexagonal ice column obtained with the boundary-element method, Applied optics 39 (30) (2000) 5541–5546.

[59] T. Y. Nakajima, T. Nakajima, K. Yoshimori, S. K. Mishra, S. N. Tripathi, Development of a light scattering solver applicable to particles of arbitrary shape on the basis of the surface-integral equations method of Müller type. I. Methodology, accuracy of calculation, and electromagnetic current on the particle surface, Applied optics 48 (19) (2009) 3526–3536.

[60] M. P. Yu, Y. P. Han, Z. W. Cui, A. T. Chen, Electromagnetic scattering by multiple dielectric particles under the illumination of unpolarized high-order Bessel vortex beam, Journal of Quantitative Spectroscopy and Radiative Transfer 195 (2017) 107–113.

[61] G. Liu, A database of microwave single-scattering properties for nonspherical ice particles, Bulletin of the American Meteorological Society 89 (10) (2008) 1563–1570.

[62] G. Hong, P. Yang, B. A. Baum, A. J. Heymsfield, F. Weng, Q. Liu, G. Heygster, S. A. Buehler, Scattering database in the millimeter and submillimeter wave range of 100–1000 GHz for nonspherical ice particles, Journal of Geophysical Research: Atmospheres 114 (D6) (2009).

[63] J. Ding, L. Bi, P. Yang, G. W. Kattawar, F. Weng, Q. Liu, T. Greenwald, Single-scattering properties of ice particles in the microwave regime: Temperature effect on the ice refractive index with implications in remote sensing, Journal of Quantitative Spectroscopy and Radiative Transfer 190 (2017) 26–37.

[64] P. Eriksson, R. Ekelund, J. Mendrok, M. Brath, O. Lemke, S. A. Buehler, A general database of hydrometeor single scattering properties at microwave and sub-millimetre wavelengths, Earth System Science Data 10 (3) (2018) 1301–1326.

[65] J. Tyynelä, J. Leinonen, D. Moisseev, T. Nousiainen, Radar backscattering from snowflakes: Comparison of fractal, aggregate, and soft spheroid models, Journal of Atmospheric and Oceanic Technology 28 (11) (2011) 1365–1372.

[66] I. Moradi, P. Stegmann, B. Johnson, V. Barlakas, P. Eriksson, A. Geer, R. Gelaro, S. Kalluri, D. Kleist, Q. Liu, et al., Implementation of a discrete dipole approximation scattering database into community radiative transfer model, Journal of Geophysical Research: Atmospheres (2022) e2022JD036957.

[67] P. G. Stegmann, G. Tang, P. Yang, B. T. Johnson, A stochastic model for density-dependent microwave snow-and graupel scattering coefficients of the noaa jcsda community radiative transfer model, Journal of Quantitative Spectroscopy and Radiative Transfer 211 (2018) 9–24.

[68] G. Tang, P. Yang, P. G. Stegmann, R. L. Panetta, L. Tsang, B. Johnson, Effect of particle shape, density, and inhomogeneity on the microwave optical properties of graupel and hailstones, IEEE Transactions on Geoscience and Remote Sensing 55 (11) (2017) 6366–6378.

[69] C. Westbrook, R. Ball, P. Field, A. Heymsfield, Theory of growth by differential sedimentation, with application to snowflake formation, Physical Review E 70 (2) (2004) 021403.

[70] A. J. Heymsfield, C. Schmitt, A. Bansemer, C. H. Twohy, Improved representation of ice particle masses based on observations in natural clouds, Journal of the Atmospheric Sciences 67 (10) (2010) 3303–3318.

[71] C. Schmitt, A. J. Heymsfield, The dimensional characteristics of ice crystal aggregates from fractal geometry, Journal of the Atmospheric Sciences 67 (5) (2010) 1605–1616.

[72] R. Cotton, P. Field, Z. Ulanowski, P. H. Kaye, E. Hirst, R. Greenaway, I. Crawford, J. Crosier, J. Dorsey, The effective density of small ice particles obtained from in situ aircraft observations of mid-latitude cirrus, Quarterly Journal of the Royal Meteorological Society 139 (676) (2013) 1923–1934.

[73] E. Erfani, D. L. Mitchell, Developing and bounding ice particle mass-and area-dimension expressions for use in atmospheric models and remote sensing, Atmospheric Chemistry and Physics 16 (7) (2016) 4379–4400.

[74] L.-H. Sun, L. Bi, B. Yi, The Use of Superspheroids as Surrogates for Modeling Electromagnetic Wave Scattering by Ice Crystals, Remote Sensing 13 (9) (2021) 1733.

[75] W. Śmigaj, T. Betcke, S. Arridge, J. Phillips, M. Schweiger, Solving boundary integral problems with BEM++, ACM Transactions on Mathematical Software (TOMS) 41 (2) (2015) 6.

[76] C. Mätzler, Microwave dielectric properties of ice, Thermal microwave radiation: applications for remote sensing 52 (2006) 455–462.

[77] V. Vouk, Projected area of convex bodies, Nature 162 (4113) (1948) 330–331.

[78] A. J. Baran, P. Connolly, C. Lee, Testing an ensemble model of cirrus ice crystals using midlatitude in situ estimates of ice water content, volume extinction coefficient and the total solar optical depth, Journal of Quantitative Spectroscopy and Radiative Transfer 110 (14-16) (2009) 1579–1598.

[79] C. Geuzaine, J.-F. Remacle, Gmsh: A 3-D finite element mesh generator with built-in pre-and post-processing facilities, International journal for numerical methods in engineering 79 (11) (2009) 1309–1331.

[80] H. Iwabuchi, P. Yang, Temperature dependence of ice optical constants: Implications for simulating the single-scattering properties of cold ice clouds, Journal of Quantitative Spectroscopy and Radiative Transfer 112 (15) (2011) 2520–2525.

[81] S. G. Warren, R. E. Brandt, Optical constants of ice from the ultraviolet to the microwave: A revised compilation, Journal of Geophysical Research: Atmospheres 113 (D14) (2008).

[82] A. Kleanthous, Accelerated calderón preconditioning for electromagnetic scattering by multiple absorbing dielectric objects, Ph.D. thesis, UCL (University College London) (2021).

[83] X. Claeys, R. Hiptmair, C. Jerez-Hanckes, Multi-trace boundary integral equations, Direct and inverse problems in wave propagation and applications 14 (2012) 51–100.

[84] X. Claeys, R. Hiptmair, Electromagnetic scattering at composite objects: a novel multi-trace boundary integral formulation, ESAIM: Mathematical Modelling and Numerical Analysis 46 (6) (2012) 1421–1445.

[85] A. Buffa, R. Hiptmair, Galerkin boundary element methods for electromagnetic scattering, in: Topics in computational wave propagation, Springer, 2003, pp. 83–124.

[86] Y. Saad, M. H. Schultz, GMRES: A generalized minimal residual algorithm for solving nonsymmetric linear systems, SIAM Journal on scientific and statistical computing 7 (3) (1986) 856–869.

[87] M. I. Mishchenko, L. D. Travis, A. A. Lacis, Scattering, absorption, and emission of light by small particles, Cambridge university press, 2002.

[88] V. I. Lebedev, Values of the nodes and weights of ninth to seventeenth order gauss-markov quadrature formulae invariant under the octahedron group with inversion, USSR Computational Mathematics and Mathematical Physics 15 (1) (1975) 44–51.

[89] V. I. Lebedev, Quadratures on a sphere, USSR Computational Mathematics and Mathematical Physics 16 (2) (1976) 10–24.

[90] V. I. Lebedev, Spherical quadrature formulas exact to orders 25–29, Siberian Mathematical Journal 18 (1) (1977) 99–107.

[91] V. I. Lebedev, A. Skorokhodov, Quadrature formulas of orders 41, 47 and 53 for the sphere, in: Russian Academy of Sciences-Doklady Mathematics, Vol. 45, 1992, pp. 587–592.

[92] V. I. Lebedev, A quadrature formula for the sphere of 59th algebraic order of accuracy, Russian Academy of Sciences-Doklady Mathematics-AMS Translation 50 (2) (1995) 283–286.

[93] V. I. Lebedev, D. Laikov, A quadrature formula for the sphere of the 131st algebraic order of accuracy, in: Doklady Mathematics, Vol. 59, Pleiades Publishing, Ltd., 1999, pp. 477–481.

[94] C. H. Beentjes, Quadrature on a spherical surface.

[95] M. I. Mishchenko, M. A. Yurkin, On the concept of random orientation in far-field electromagnetic scattering by nonspherical particles, Optics letters 42 (3) (2017) 494–497.

[96] M. I. Mishchenko, Calculation of the amplitude matrix for a nonspherical particle in a fixed orientation, Applied optics 39 (6) (2000) 1026–1031.

[97] M. Brath, R. Ekelund, P. Eriksson, O. Lemke, S. A. Buehler, Microwave and submillimeter wave scattering of oriented ice particles, Atmospheric Measurement Techniques 13 (5) (2020) 2309–2333.

[98] I. Fenni, K.-S. Kuo, M. S. Haynes, Z. S. Haddad, H. Roussel, Evaluation of higher-order quadrature schemes in improving computational efficiency for orientation-averaged single-scattering properties of nonspherical ice particles, Journal of Geophysical Research: Atmospheres 126 (11) (2021) e2020JD034172.

[99] M. A. Yurkin, Fair evaluation of orientation-averaging techniques in light-scattering simulations: Comment on "evaluation of higher-order quadrature schemes in improving computational efficiency for orientation-averaged single-scattering properties of nonspherical ice particles" by fenni et al, Journal of Geophysical Research: Atmospheres 128 (2) (2023) e2021JD036088.

[100] M. W. Scroggs, T. Betcke, E. Burman, W. Śmigaj, E. van't Wout, Software frameworks for integral equations in electromagnetic scattering based on Calderón identities, Computers & Mathematics with Applications 74 (11) (2017) 2897–2914.

[101] L. Rayleigh, V. On the incidence of aerial and electric waves upon small obstacles in the form of ellipsoids or elliptic cylinders, and on the passage of electric waves through a circular aperture in a conducting screen, The London, Edinburgh, and Dublin Philosophical Magazine and Journal of Science 44 (266) (1897) 28–52.

[102] M. I. Mishchenko, L. D. Travis, Capabilities and limitations of a current FORTRAN implementation of the T-matrix method for randomly oriented, rotationally symmetric scatterers, Journal of Quantitative Spectroscopy and Radiative Transfer 60 (3) (1998) 309–324.

[103] J. Gasteiger, M. Wiegner, Mopsmap v1. 0: a versatile tool for the modeling of aerosol optical properties, Geoscientific Model Development 11 (7) (2018) 2739–2762.

[104] F. Kanngießer, M. Kahnert, Modeling optical properties of non-cubical sea-salt particles, Journal of Geophysical Research: Atmospheres 126 (4) (2021) e2020JD033674.

[105] A. Virkki, K. Muinonen, A. Penttilä, Radar albedos and circular-polarization ratios for realistic inhomogeneous media using the discrete-dipole approximation, Journal of Quantitative Spectroscopy and Radiative Transfer 146 (2014) 480–491.

[106] B. T. Draine, P. J. Flatau, DDSCAT: The discrete dipole approximation for scattering and absorption of light by irregular particles, Astrophysics Source Code Library (2000) ascl–0008.

[107] M. A. Yurkin, A. G. Hoekstra, The discrete-dipole-approximation code adda: capabilities and known limitations, Journal of Quantitative Spectroscopy and Radiative Transfer 112 (13) (2011) 2234–2247.